

1854-3

**Crack Width Prediction for Interior Portion
of Inverted 'T' Bent Caps**

**Prepared for
Texas Department of Transportation**

**By
Rong-Hua Zhu
Wirat Wanichakorn
and
Thomas T. C. Hsu**

**Department of Civil and Environmental Engineering
University of Houston
Houston, Texas**

August 2001

1. Report No. TxDOT 0-1854-3		2. Government Accession No.		3. Recipient's Catalog No.	
4. Title and Subtitle Crack Width Prediction for Interior Portion of Inverted 'T' Bent Caps				5. Report Date August 2001	
				6. Performing Organization Code	
7. Author(s) Rong-Hua Zhu, Wirat Wanichakorn, Thomas T. C. Hsu				8. Performing Organization Report No. 1854-3	
9. Performing Organization Name and Address Department of Civil & Environmental Engineering Cullen College of Engineering University of Houston 4800 Calhoun Rd. Houston, TX 77204-4793				10. Work Unit No. (TRAIS)	
				11. Contract or Grant No. 0-1854	
12. Sponsoring Agency Name and Address Texas Department of Transportation Research and Technology Implementation Office P. O. Box 5080 Austin, Texas 78763-5080				13. Type of Report and Period Covered Research Report	
				14. Sponsoring Agency Code	
15. Supplementary Notes Project conducted in cooperation with the Texas Department of Transportation and the U.S. Department of Transportation, Federal Highway Administration.					
16. Abstract <p>Inverted "T" bent caps are used extensively in highway bridges to support elevated roadways on beams. Such bent caps are esthetically pleasing as well as economically sound. The cross-section of an inverted "T" bent cap consists of a "web" (or "stem") with short cantilever "ledges" at the bottom to support the beams, thus minimizing the structural depth of bridges. At service load unacceptable diagonal cracking frequently occurs between the cantilever ledges and the web.</p> <p>An important factor contributing to this cracking is the lack of a rational behavioral theory that supports serviceability design of such bent caps. Current design guidelines are based on the ultimate load stage and do not address cracking at service load (AASHTO, 1996; ACI, 95; Mirza and Furlong, 1985). Thus, it is necessary to develop a serviceability design method that takes into account the deformation compatibility condition because any method that attempts to determine crack width must consider strains in both the concrete and the steel. To this end, we have taken the following approach: First, develop a compatibility-aided struts-and-ties model that leads to a simple design method capable of controlling crack widths at service load; and second, conduct experimental tests on full-sized specimen and use the test results to calibrate the theoretical model.</p> <p>The study of inverted 'T' bent caps involves the testing and analysis of two types of specimens. The first type of specimen represents approximately an interior slice of the inverted 'T' bent cap. It is proposed that this slice be treated as a 2-dimensional problem by converting the two loads on the ledges into line loads and by placing the center reaction as a line load directly on the bottom surface of the web. This simplification allows us to develop a 2-D CASTM rather than a 3-D CASTM. The loading condition of a 2-D test specimen happens to represent closely the loading condition at the dapped end of a bridge girder.</p> <p>The second type of specimens represents the end portion of an inverted 'T' bent cap. The stresses and strains in the end portion are 3-dimensional.</p> <p>This report summarizes the first phase of this effort, i.e. the tests and analyses of seven 2-D specimens—BPC1, T2, T3, T4, T5, T6, and T7. It describes (1) the experiments and the test results of the seven full-sized specimens simulating the interior portions of an inverted "T" bent cap; and (2) the development of a 2-D compatibility-aided struts-and-ties model (CASTM) that is applicable to inverted "T" bent caps with and without diagonal bars at the re-entrant corner. The proposed formulas for predicting crack widths at service load are quite simple and conceptually very clear. The second phase of the research, i.e. the tests and analyses of 3-D specimens, is currently under way. The test results and the CATSM for 3-D specimens will be presented in a separate report.</p>					
17. Key Words			18. Distribution Statement No restrictions. This document is available to the public through NTIS: National Technical Information Service 5285 Port Royal Road Springfield, Virginia 22161		
19. Security Classif.(of this report) Unclassified		20. Security Classif.(of this page) Unclassified		21. No. of Pages 66	22. Price

**Research Report 0-1854-3
to
Texas Dept. of Transportation
Project 0-1854**

**Crack Width Prediction for
Interior Portion of Inverted 'T' Bent Caps**

by

Rong-Hua Zhu, Research Associate
Wirat Wanichakorn, Research Assistant
Thomas T. C. Hsu, Moores Professor

Dept. of Civil & Environmental Engineering
Cullen College of Engineering
University of Houston

Aug. 1, 2001

1. INTRODUCTION

1.1 Research Objectives

Inverted "T" bent caps are used extensively in highway bridges to support elevated roadways on beams. Such bent caps have appeal because they are esthetically pleasing as well as economically sound. The cross-section of an inverted "T" bent cap consists of a "web" (or "stem") with short cantilever "ledges" at the bottom to support the beams, thus minimizing the structural depth of bridges. At service load unacceptable diagonal cracking frequently occurs between the cantilever ledges and the web.

An important factor contributing to the observed cracking is the lack of a rational behavioral theory that supports serviceability design of such bent caps. Current design guidelines are based on the ultimate load stage and do not address cracking at service load (AASHTO, 1996; ACI, 95; Mirza and Furlong, 1985). Thus, it is necessary to develop a serviceability design method that takes into account the deformation compatibility condition because any method that attempts to determine crack width must consider strains in both the concrete and the steel. To this end, we have taken the following approach: First, develop a compatibility-aided struts-and-ties model that leads to a simple design method capable of controlling crack widths at service load; and second, conduct experimental tests on full-sized specimen and use the test results to calibrate the theoretical model.

1.2 Test Specimens for Inverted 'T' Bent Caps

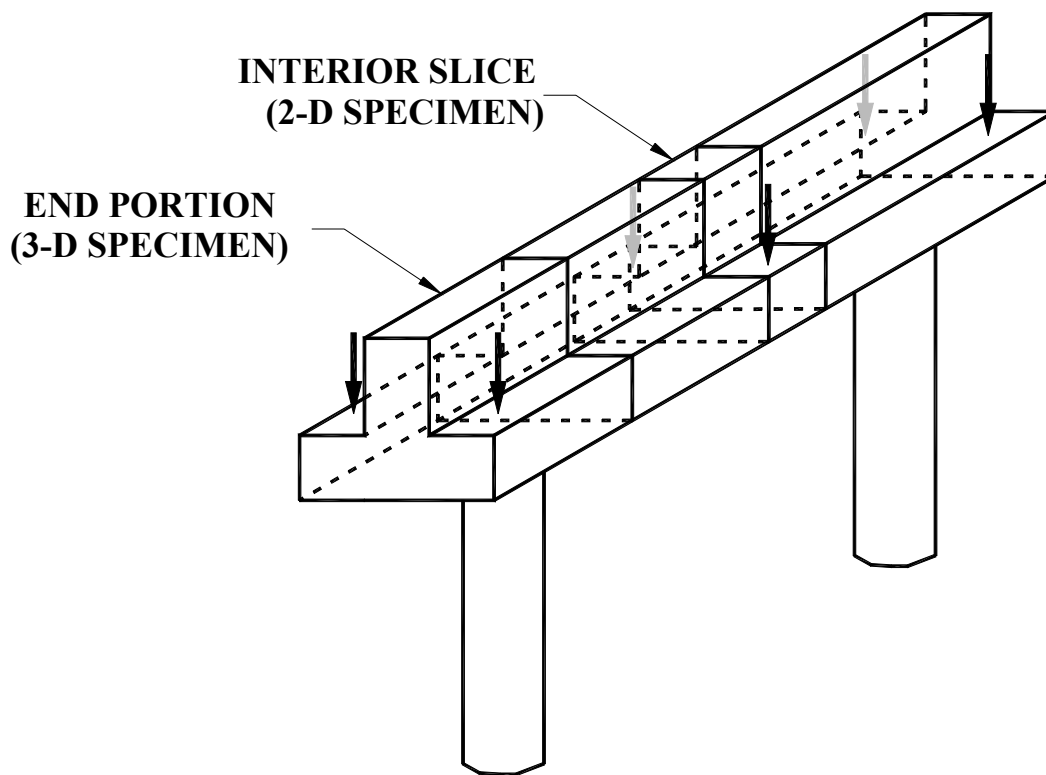
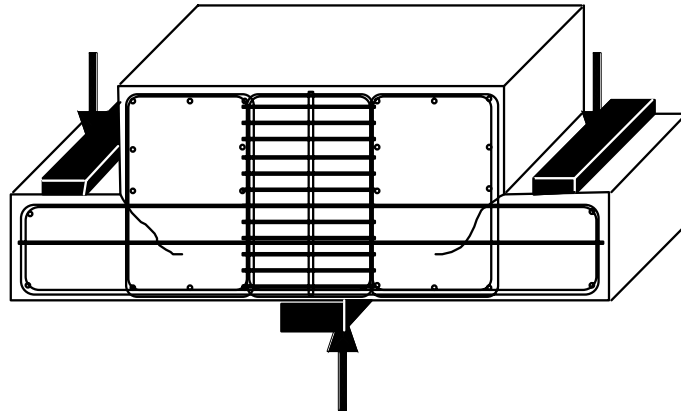


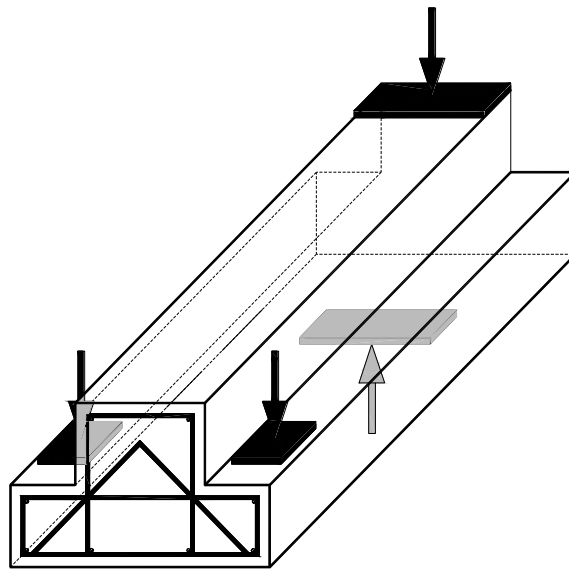
Fig. 1.1 An Inverted 'T' bent cap showing an interior slice (2-D specimen) and an exterior portion (3-D specimen).

The study of inverted 'T' bent caps, as shown in Fig. 1.1, involves the testing and analysis of two types of specimens. The first type of specimen, as shown in Fig. 1.2 (a), represents approximately an interior slice of the inverted 'T' bent cap. It is proposed that this slice be treated as a 2-dimensional problem by converting the two loads on the ledges into line loads and by placing the center reaction as a line load directly on the bottom surface of the web. This simplification allows us to develop a 2-D CASTM rather than a 3-D CASTM. The loading condition of a 2-D test specimen happens to represent closely the loading condition at the dapped end of a bridge girder.

The second type of specimens, as shown in Fig. 1.2 (b), represents the end portion of an inverted 'T' bent cap. The stresses and strains in the end portion are 3-dimensional.



(a) 2-D test specimens



(b) 3-D test specimens

Fig. 1.2 2-D vs. 3-D test specimens

1.3 Scope of This Report

This report summarizes the first phase of this effort, i.e. the tests and analyses of seven 2-D specimens --- BPC1, T2, T3, T4, T5, T6, and T7. It describes (1) the experiments and the test results of the seven full-sized specimens simulating the interior portions of an inverted "T" bent cap; and (2) the development of a 2-D compatibility-aided struts-and-ties model (CASTM) that is applicable to inverted "T" bent caps with and without diagonal bars at the re-entrant corner. The proposed formulas for predicting crack widths at service load are quite simple and conceptually very clear.

The second phase of the research, i.e. the tests and analyses of 3-D specimens, is currently under way. The test results and the CATSM for 3-D specimens will be presented in a separate report.

2. EXPERIMENTS

2.1 2-D Specimens Tested

The design and steel arrangement of the seven test specimens are summarized in Table 2.1 and in the following Fig. 2.1 (a) to (g). 2-D test specimens are symmetrical about their centerlines so that each specimen can furnish two tests, one on the left and one on the right.

Table 2.1 Steel Arrangement and Experimental Loads in Test Specimens

Specimen	f'_c (psi)	Number of Bars				Ultimate Load (kips)	Service Load (kips)
		Hanger	Flexural	Diagonal	Shear		
BPC1	5,730	6	5	0	3	N/A	198-226
T2	6,054	3	3	0	2	253	94-106
T3	4,865	5	3	0	2	242	111-143
T4	6,011	3	5	0	0	257	111-135
T5	5,649	3	3	3	0	414	128-183
T6	6,283	5	3	0	0	210	104-124
T7	6,826	3	3	5	0	538	167-233

The service load is defined as a range from 60% of the first yield load to 60% of the last yield load. In the case where none of the steel bars yielded, the ultimate load will be used as the last yield load. The yield loads of hanger steel, flexural steel and diagonal steel are determined from the SR4 electrical strain gauges when the largest strain reaches 0.0022 (for yield strength of 64,000 psi).

Specimen BPC1 (see First Annual Report, Nov. 30, 1999) was planned for two special objectives. First, it was used to check for the validity of the instrumentation method, and second, it was used to study a new repair method using carbon fiber sheets. To achieve the second objective, the specimen was loaded up to the yield point and then unloaded. The cracked specimen was repaired by carbon fiber sheets, and then loaded to failure. As such, no ultimate load could be obtained for the specimen itself.

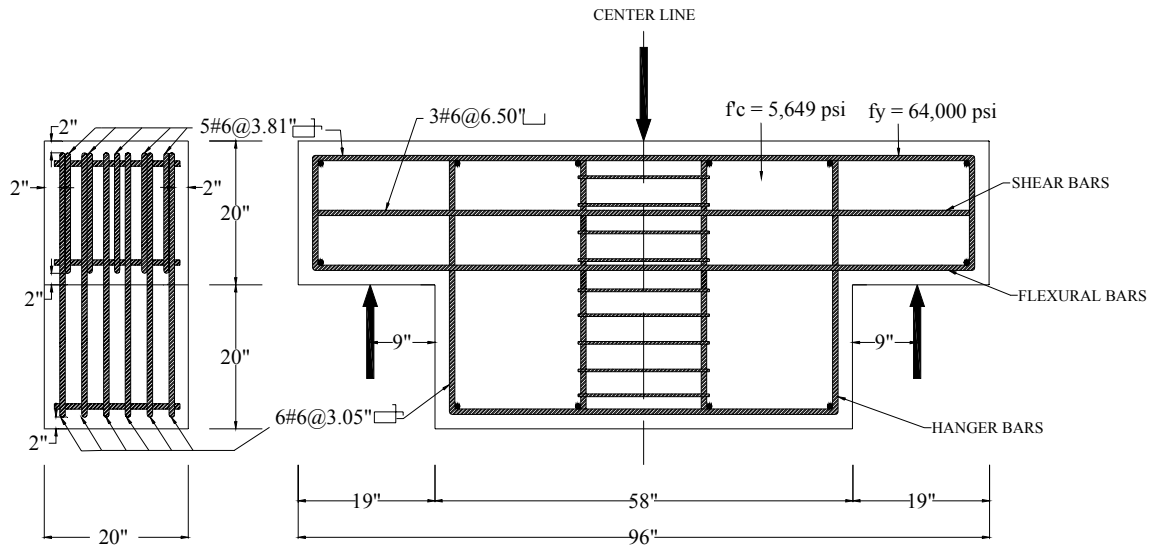


Fig. 2.1 (a) Steel Arrangement and Dimension of Specimen BPC1

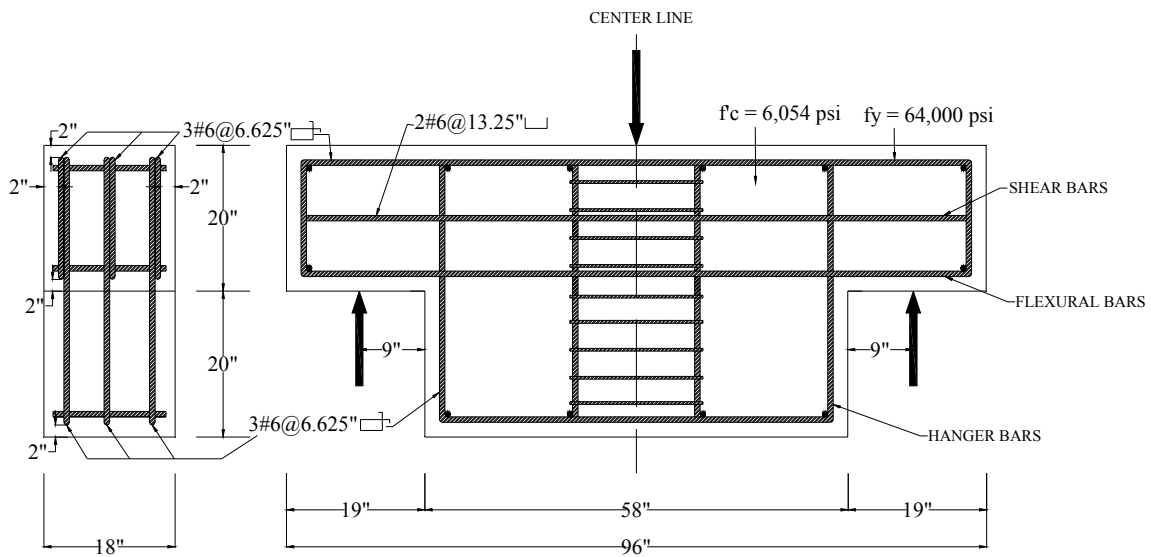


Fig. 2.1 (b) Steel Arrangement and Dimension of the Specimen T2

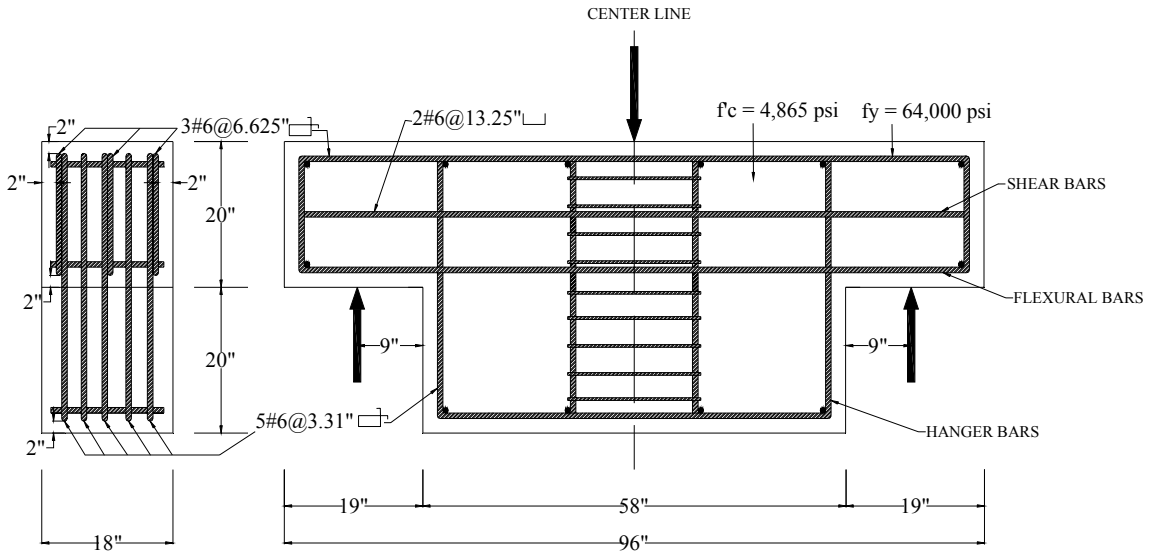


Fig. 2.1 (c) – Steel Arrangement and Dimension of Specimen T3

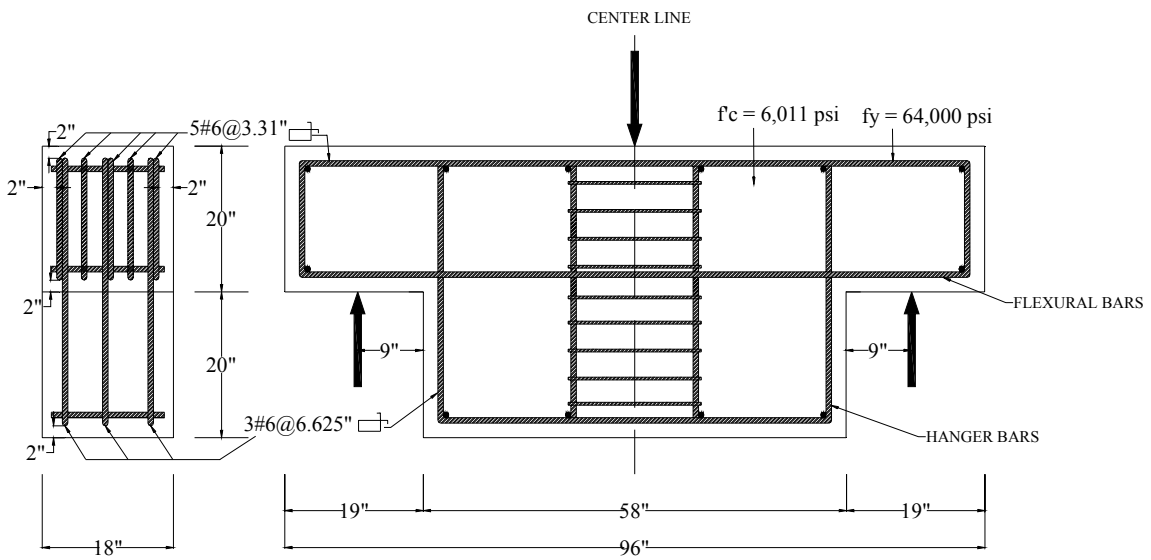


Figure 2.1 (d) – Steel Arrangement and Dimension of Specimen T4

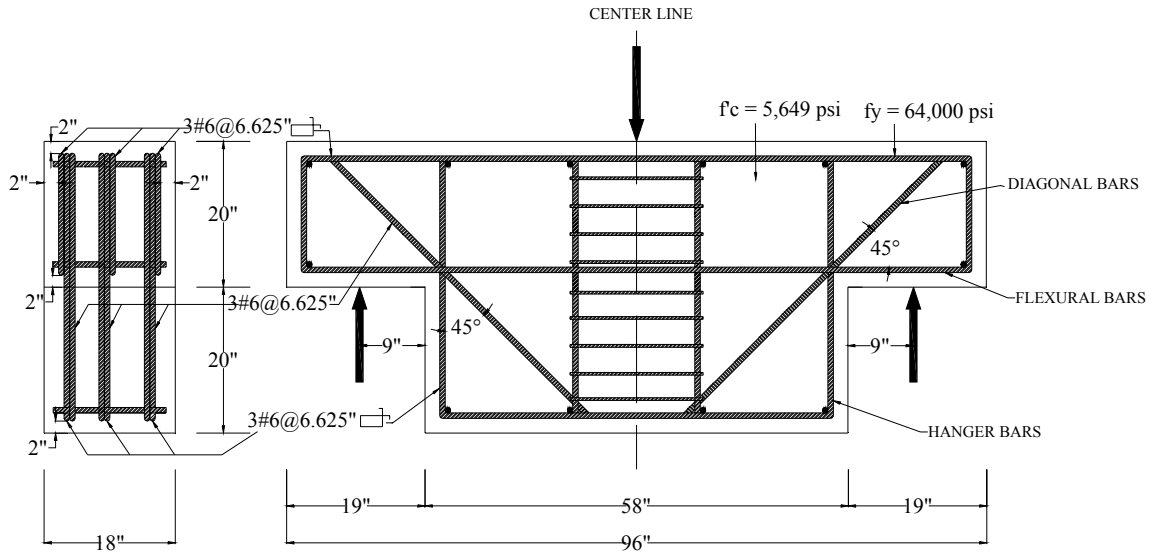


Fig. 2.1 (e) – Steel Arrangement and Dimension of Specimen T5

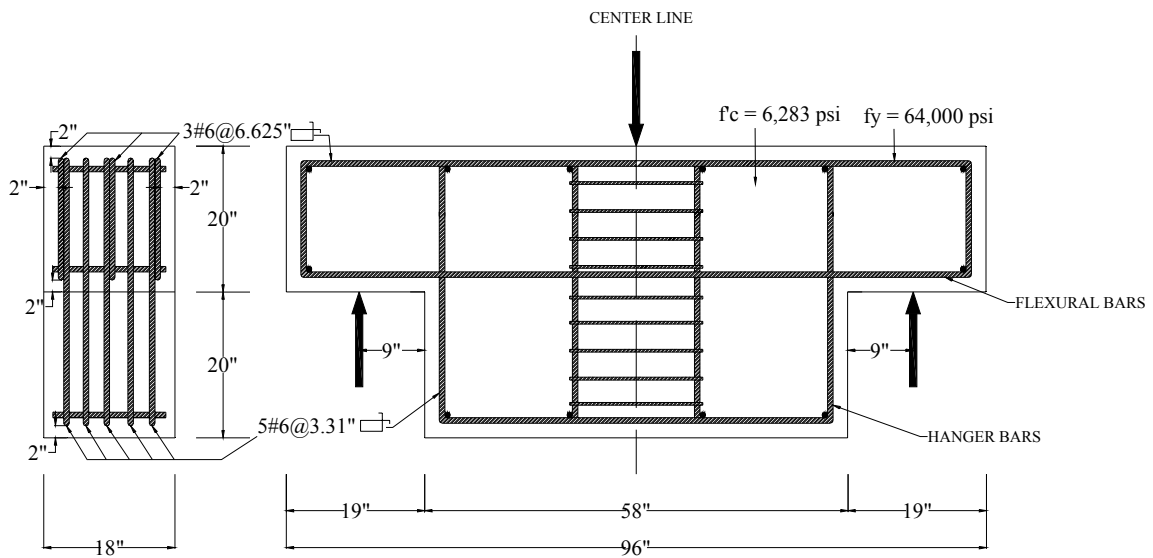


Fig. 2.1 (f) – Steel Arrangement and Dimension of Specimen T6

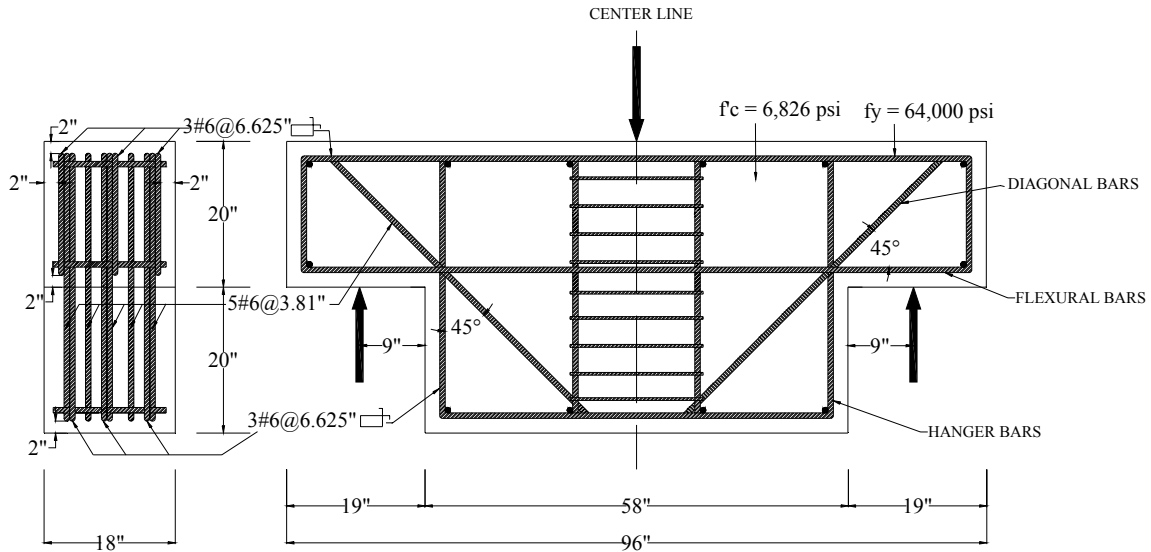


Fig. 2.1 (g) – Steel Arrangement and Dimension of Specimen T7

2.2 Materials

2.2.1 Concrete

The concrete used in the test specimens must be similar to the concrete of the inverted T-beams. For this reason it was decided to use the class “F” six-sack concrete mix with a compressive strength of 5000 psi or more. Because of the large size of the specimen, it was also decided to use ready-mixed concrete rather than mixing the concrete in our own laboratory. In order to ensure the quality and consistency of the concrete, the mix proportion was decided jointly with the supplier based on TXDOT specifications as follows:

Type 1 Portland Cement -398 lbs;

Limestone aggregate (1” max.)- 1573 lbs;

Sand - 1391 lbs;

Fly ash -132 lbs;

Water -250 lbs;

Slump - 3.5-5";

Compressive strength -5730 psi.

The compressive strength of concrete was obtained by testing 6 by 12 standard concrete cylinders. The stress-strain curves of standard concrete cylinders from Specimen BPC1 are shown in Fig. 2.2 (a).

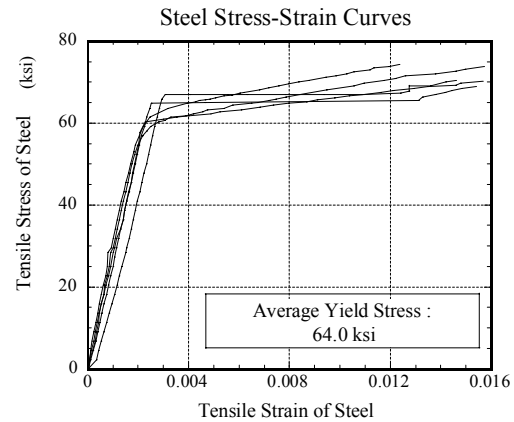
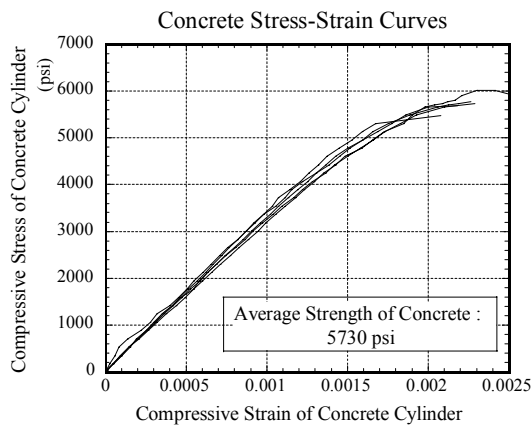


Fig. 2.2(a) Compressive stress-strain curves of concrete

Fig. 2.2(b) Tensile stress-strain curves of

2.2.2 Steel

Grade 60 rebars were used. The stress-strain curves of steel bar are shown in Fig.2.2 (b). With an average yield stress of 64.0 ksi, the corresponding yield strain is 0.0022.

2.3 Test Facility

2.3.1 Loading System

All specimens were tested in the 2.5-million lbs MTS testing system as shown in Fig. 2.3. This MTS test system was controlled by a versatile TestStar system, which could provide not only load-control procedure but also strain-control procedure. External load was applied at the center of the specimen. A continuous record of the stresses and strains was obtained by applying the forces (load control) or the deformations (strain control) during the test.



Fig. 2.3 The MTS Test System and Testing Facility

2.3.2 Instrumentation and Data Acquisition

A total of 38 LVDTs and 24 SR4 electrical strain gauges were used for testing each specimen. The average strains of concrete and steel were measured on the surface of the specimen by 14 linear voltage displacement transducers (LVDTs) as shown in Fig. 2.4. The geometric layout and the labeling of the LVDTs are shown in Fig. 2.5 (a) to (d).

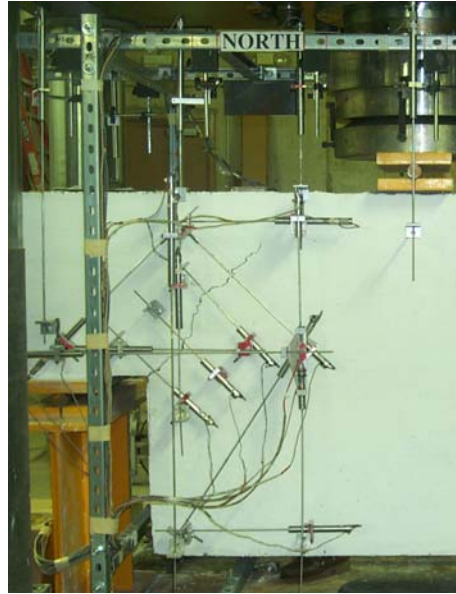


Fig. 2.4 The Layout of LVDTs

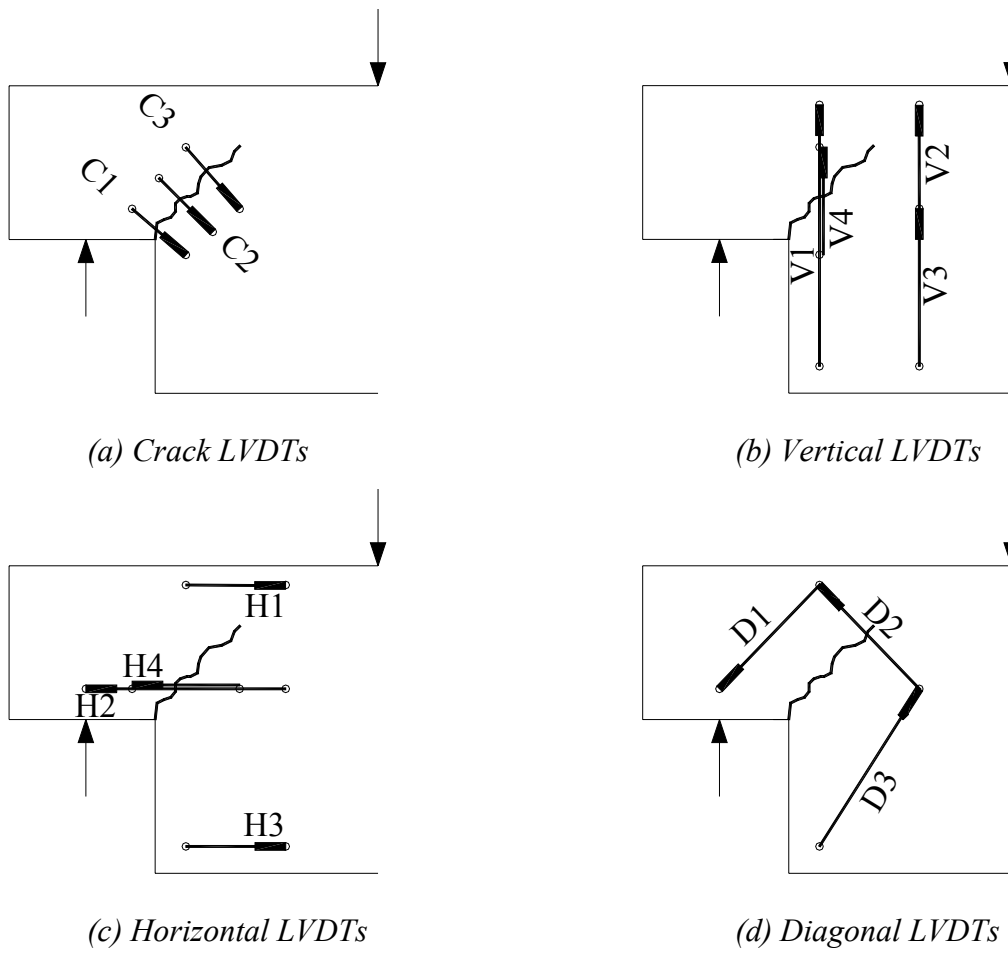


Fig. 2.5 Arrangement of LVDTs in each Direction

The LVDTs were arranged in a pattern according to the proposed strut-and-tie model and in such a way that the strain data can be cross-checked.

The local strains on the hanger steel, the flexural steel, diagonal steel, and the shear steel were measured by 6 mm SR4 electrical strain gauges attached to the steel bars as shown in Fig. 2.6. The location and the spacing of the gauges are shown later in Fig. 3.9.

Fig. 2.7 shows a 64-channel HBM Spider 8 data acquisition system. The HBM Spider 8 system is a new type of data acquisition system for parallel, dynamic measurement. These characteristics are desirable in the future for cyclic loading tests simulating repeated vehicle loading. This new instrument is also more versatile, because each of the 64 channels can accept both the high-voltage signals from LVDTs and the low-voltage signals from SR4 gauges. To utilize this versatility, 80 cables (40 for LVDTs and 40 for SR4 gauges) with connectors consistent with the new acquisition system were manufactured as shown in Fig. 2.8.

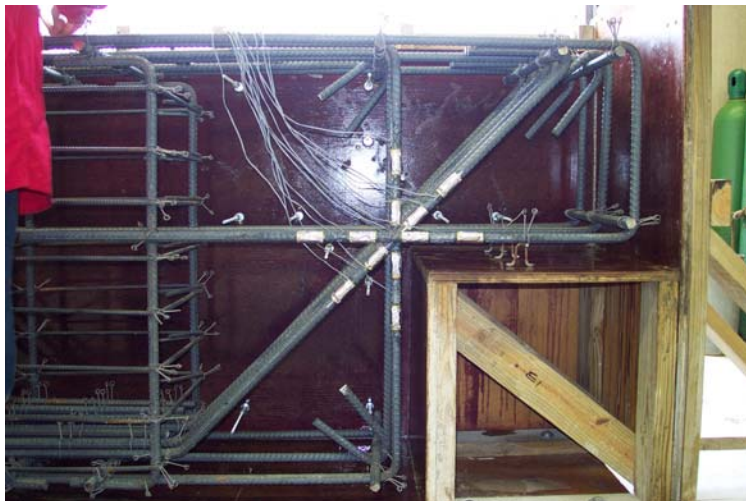


Fig. 2.6 The Attachment of SR4 Electrical Strain Gauges



Fig. 2.7 The HBM Spider 8 Data Acquisition System



Fig. 2.8 Components of Data Acquisition System

2.3.3 Deflection measurements and Bearing Pads

2.3.3.1 Specimen BPC1

Six LVDTs were used for measuring the deflected shape of the loaded specimen as shown in Fig. 2.9. The vertical deflections of the specimens were measured with respect to the movable crosshead assuming the whole MTS test frame to be rigid during testing. This assumption of using the MTS test frame as a reference frame was found to be erroneous.

To simulate real applications of inverted ‘T’ bent caps, a piece of rectangular rubber bearing pad was placed between the ledge of the specimen and the support. The purpose of using the rubber pads was to make certain that the reactions from the supports were distributed uniformly along the entire width of the specimen. After testing, however, it was found that the pads were too soft, and thicker, stiffer rubber pads were used in the testing of Specimen T2.

2.3.3.2 Specimen T2

The test results of Specimen BPC1 showed that the deflection measurements were unreasonable because the MTS machine did not act as a rigid frame as previously thought. The upper movable crosshead slipped against its 4 columns as the applied load increased. A new reference frame was then constructed for the testing of later specimens. The new reference frame was fixed to the base plate of the MTS machine, on which the specimen was supported. Fig. 2.10 shows the new reference frame.

Although the vertical displacement measured by LVDTs E1, E2, E3, W1, W2, W3 in Fig. 2.10 are correct, an error was made in the measurement of the vertical

displacement at midspan. As a result, the load-displacement curve at midspan is not included in Fig. 3.1.

The rubber-bearing pads used in the testing of Specimen T2 were thicker and stiffer than those used in Specimen BPC1. However, they were still too soft for the load applied to Specimen T2. It also appeared that the rubber-bearing pads contributed to the inaccurate measurement of the vertical deflections. For these reasons, rubber-bearing pads were not used in the testing of Specimens T3 to T7.

2.3.3.3 Specimen T3-T7

After evaluating the results of Specimen T2, it was decided that 10 LVDTs were needed to measure the deflected shape of Specimens T3, T4, T5, T6, and T7. Instead of connecting the LVDTs from the reference frame to the top surface of the specimens, the LVDT rods were connected from the reference frame to the threaded rods that are anchored into the concrete on the side faces of the specimens. Fig. 2.11 shows the new layout of the LVDTs (E1 to E5 and W1 to W5) for measuring the vertical deflection of these specimens. The real vertical deflection curve of the specimen could then be accurately determined by subtracting the average deflections measured by LVDTs at the supports (E1, E5, W1, and W5) from the LVDTs measurements at other locations (E2, E3, E3, W2, W3, and W4).

Instead of rubber-bearing pads, cement paste was used to distribute the reaction force from each support into the ledge of a specimen.

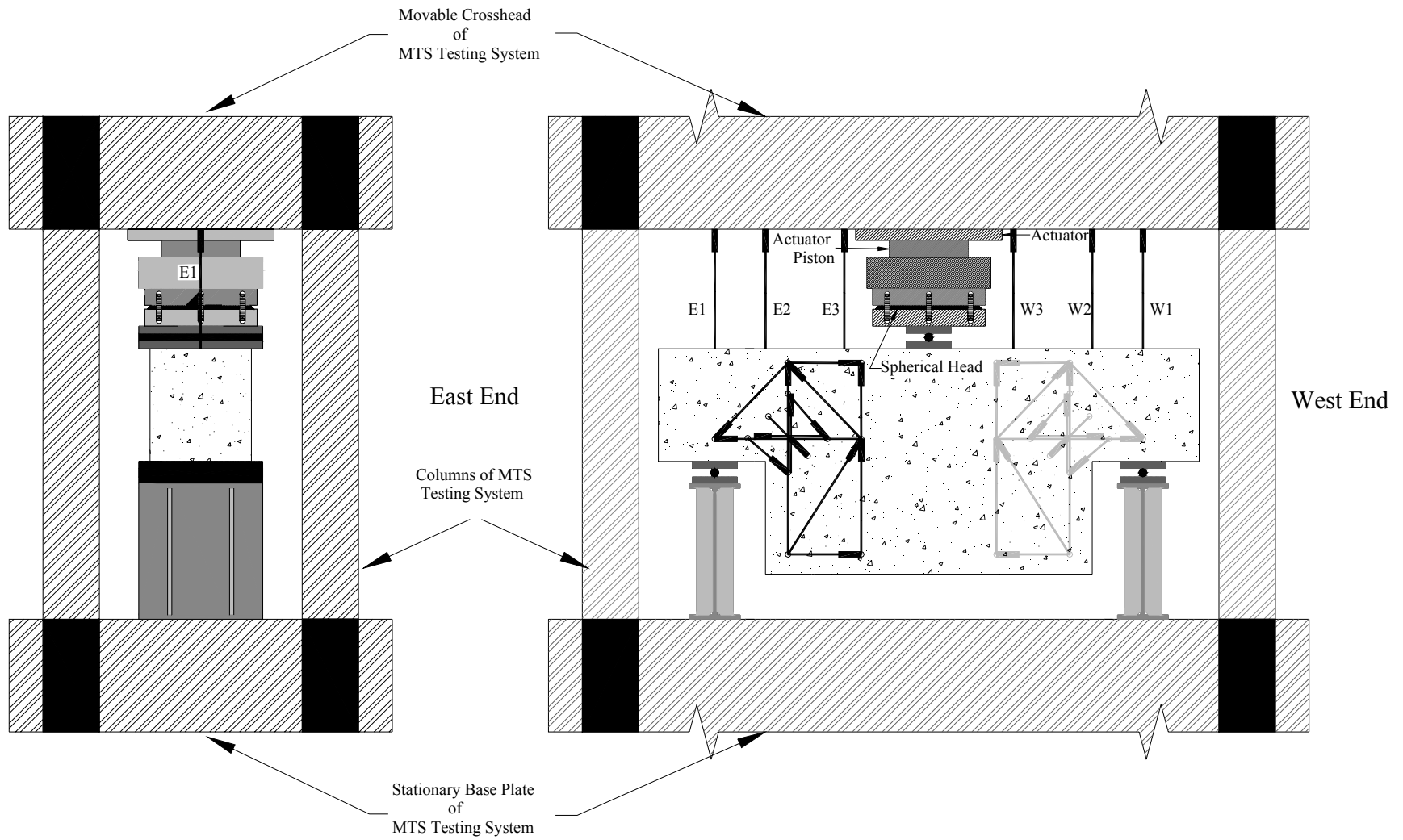


Fig. 2.9 Reference Frame and LVDT Arrangement of Specimen BPC1

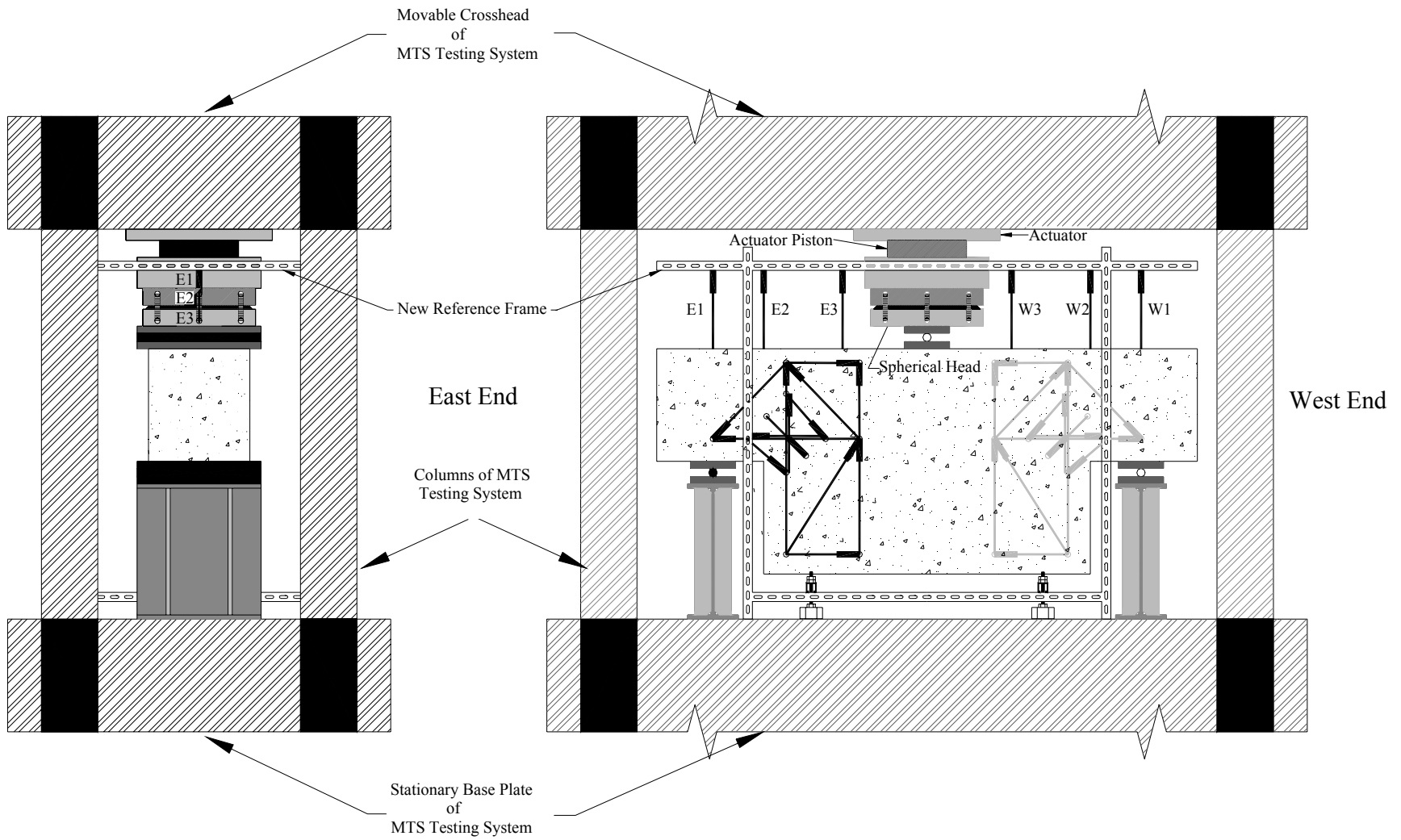


Fig.2.10 New Reference Frame and LVDT Arrangement of Specimen T2

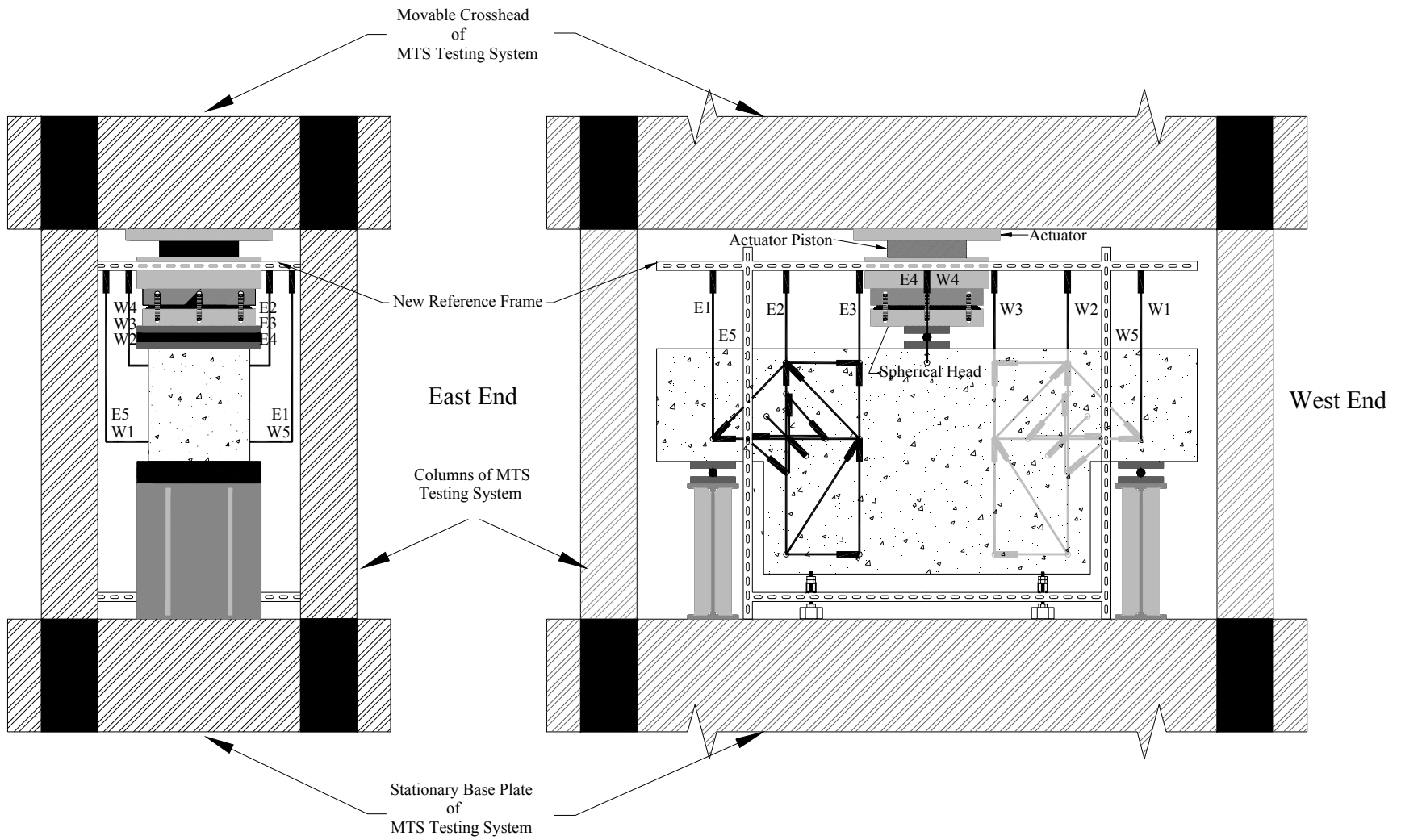


Fig.2.11 Reference Frame and LVDT Arrangement of Specimen T3-T

3. TEST RESULTS

Test results of Specimen BPC1, T2, T3, T4, T5, T6, and T7 are summarized in this section.

3.1 Load-displacement Curves

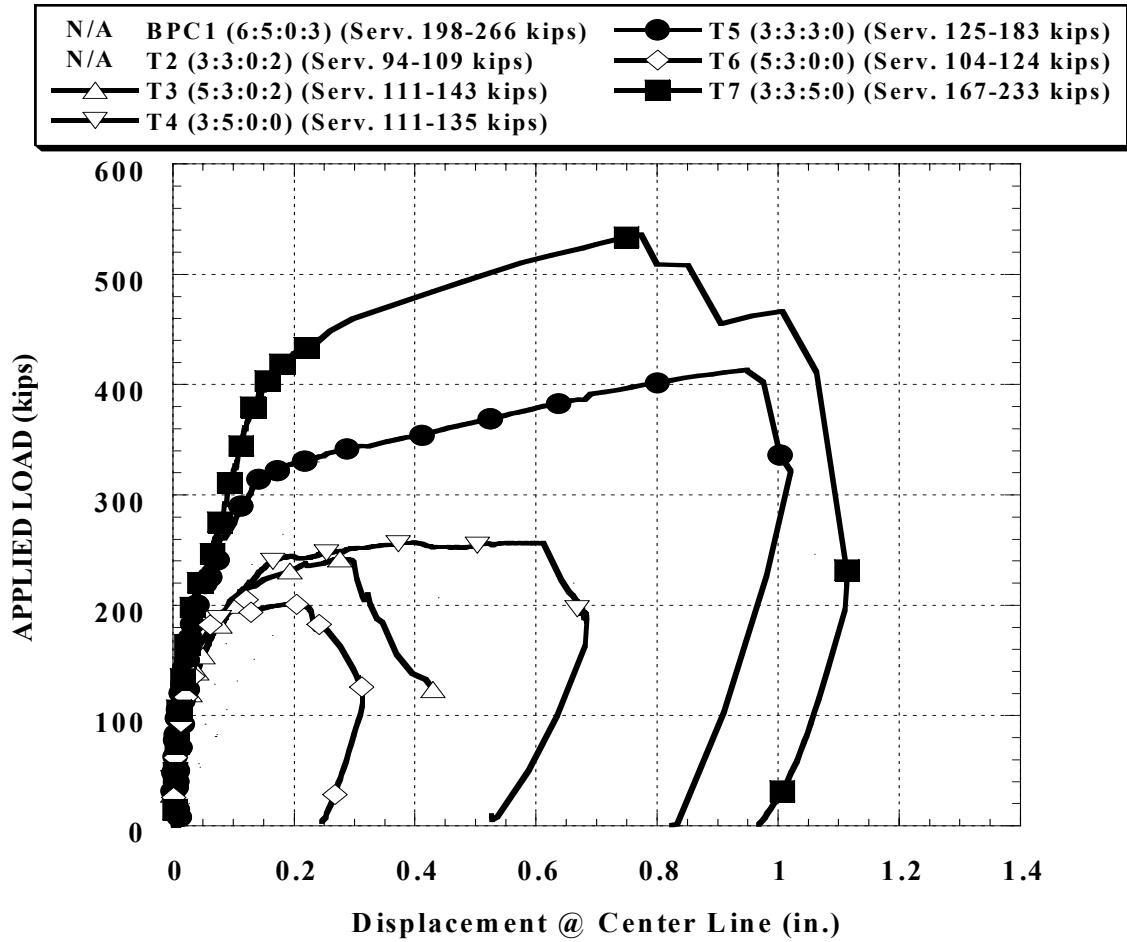


Fig. 3.1 Load-displacement Curves of Specimen T3-T7

The load-displacement curves of Specimen T3 to T7 are shown in Fig. 3.1. In this figure, the vertical axis represents the applied load at the center of the specimen, and the horizontal axis represents the corresponding displacement at the center of the specimen. The legend in the figure indicates the number of No. 6 steel bars used for each type of reinforcement in the following sequence: (hanger steel: flexural steel: diagonal steel:

shear-friction steel). The service load ranges of the six specimens are also shown. The service load range is defined as a range from 60% of the first yield load to 60% of the last yielding. The yield loads were determined by measurements of SR4 strain gauges placed on all four types of reinforcement.

The ultimate capacities and the ductilities of the six specimens can be compared using Fig. 3.1. For example, Specimen T5, with numbers of No. 6 steel bars indicated by (3:3:3:0), has 30% less ultimate capacity and approximately 46% more ductility than Specimen T7 (3:3:5:0).

3.2 Crack Patterns

Fig. 3.2 to 3.7 show the crack patterns on the North faces of Specimen T2 to T7 at their respective service loads. It can be seen than one single crack appears at each re-

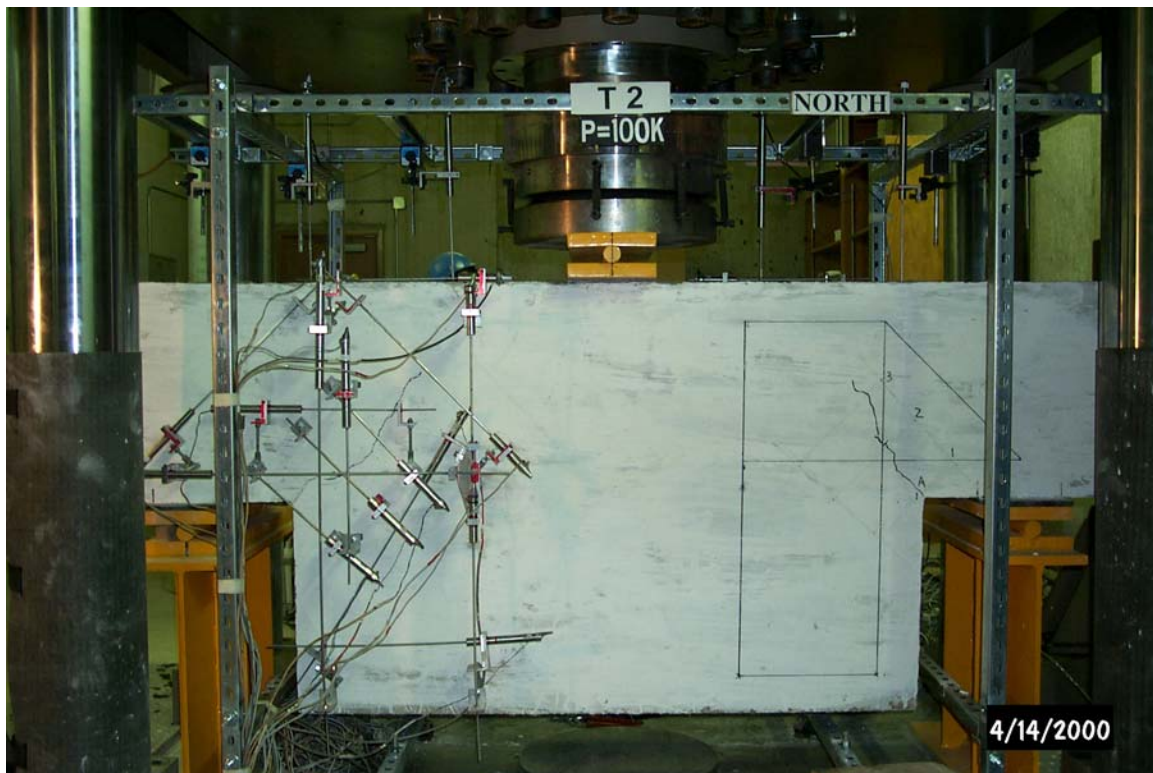


Fig. 3.2 Crack Pattern of Specimen T2 at Service Load

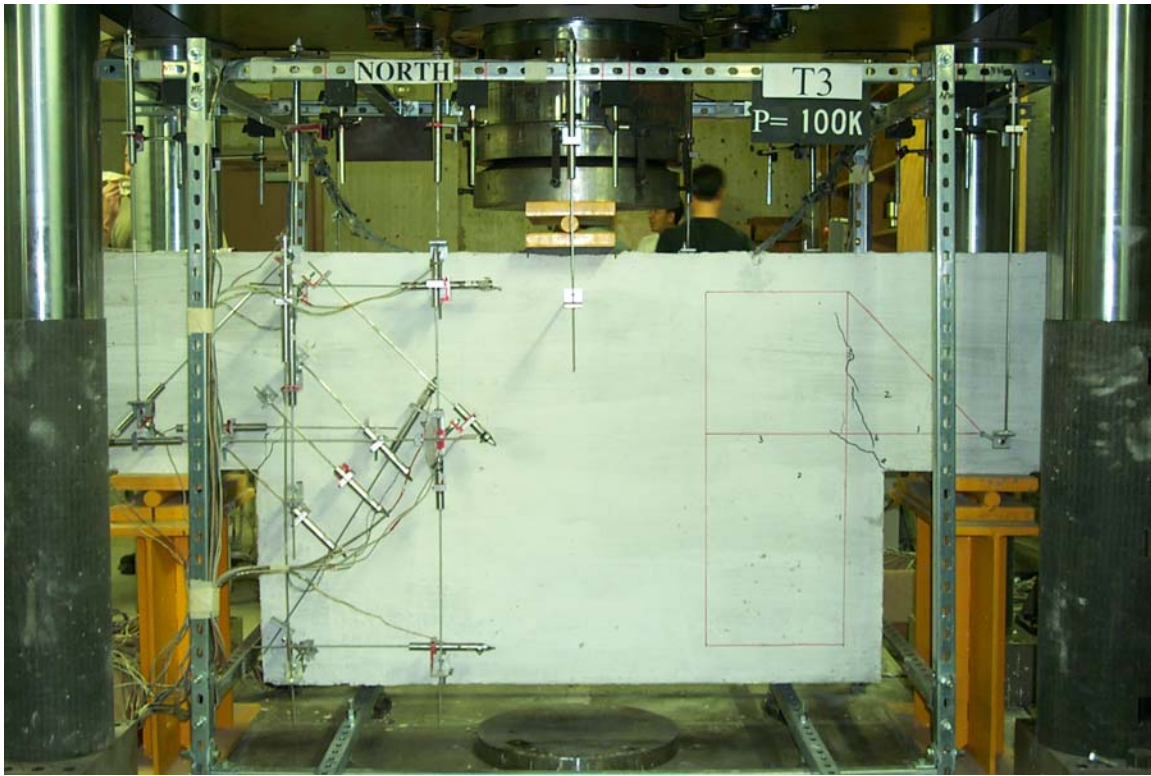


Fig. 3.3 Crack Pattern of Specimen T3 at Service Load

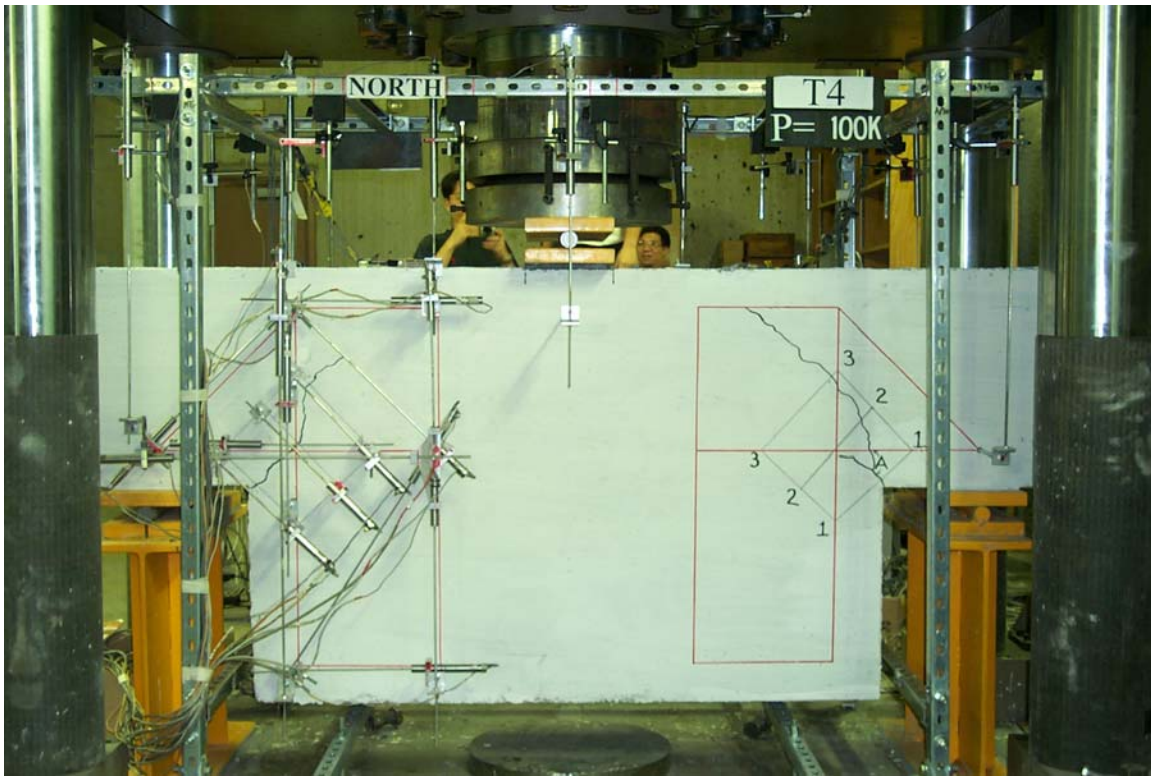


Fig. 3.4 Crack Pattern of Specimen T4 at Service Load

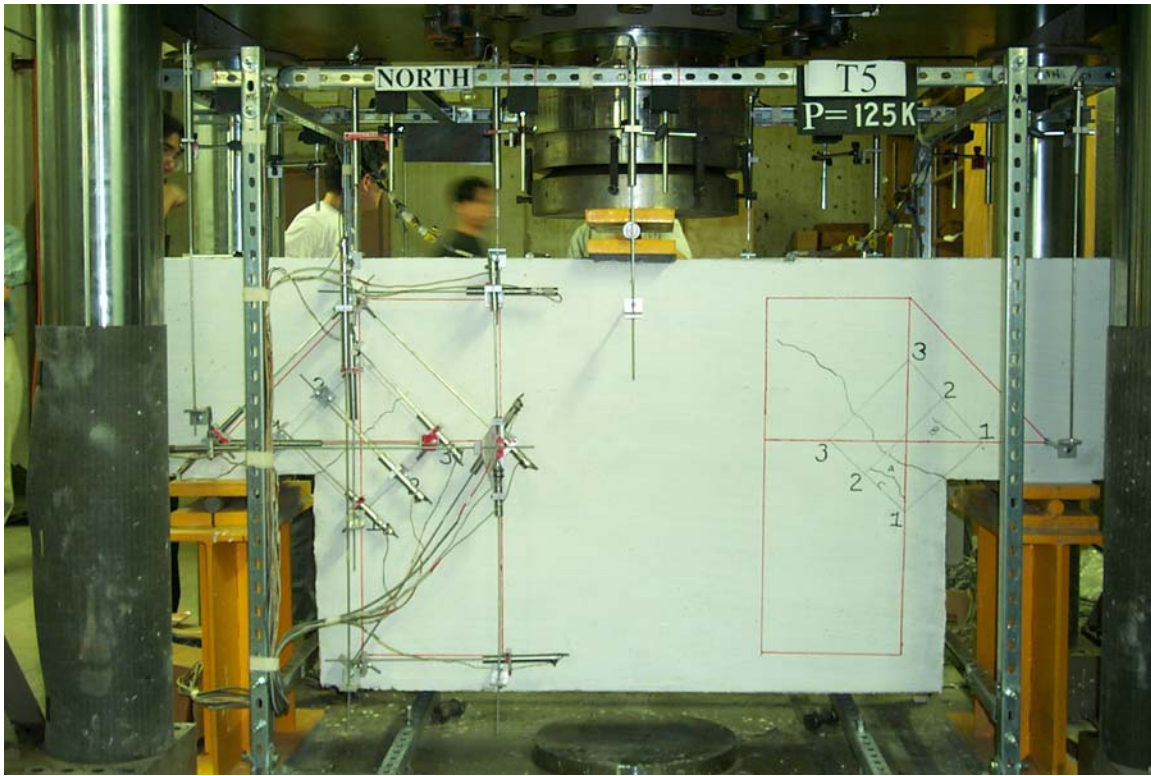


Fig. 3.5 Crack Pattern of Specimen T5 at Service Load

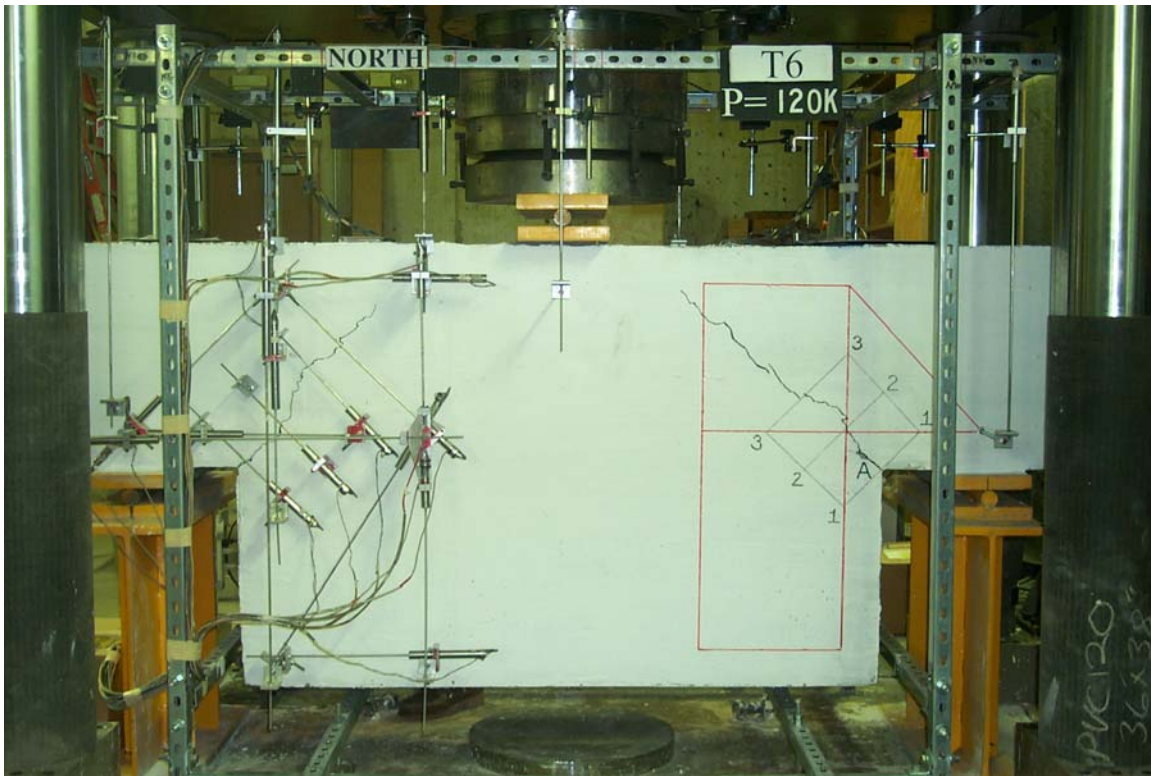


Fig. 3.6 Crack Pattern of Specimen T6 at Service Load

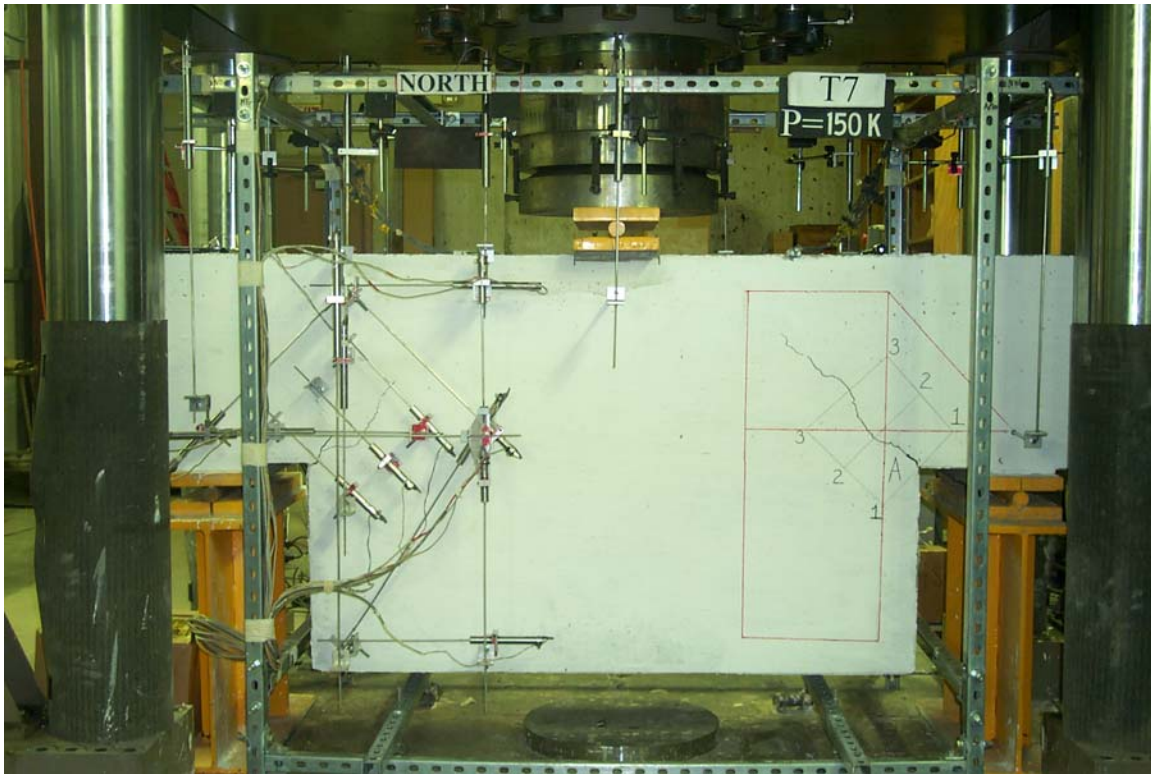


Fig. 3.7 Crack Pattern of Specimen T7 at Service Load

entrant corner of each specimen. The first crack of each specimen appears when the applied load is in the range of 35-70 kips depending on the compressive strength of concrete and the amount of reinforcement used. The average angle of crack of all specimens with respect to the re-entrant corner is, approximately, 45 degree.

3.3 Diagonal Crack Strains Measured from LVDTs

The measured diagonal crack strains for Specimen T2 to T7 are plotted in Fig. 3.8 using LVDTs. The horizontal axis indicates the applied load measured by the MTS load cell on the loading piston. The vertical axis indicates the average strain (LVDTs C1 to C3) of the diagonal crack in the vicinity of the two re-entrant corners of each specimen. Since the effects of different steel proportions are being studied in order to control crack

width, the effects of diagonal, hanger, flexural, and shear-friction reinforcement will be discussed.

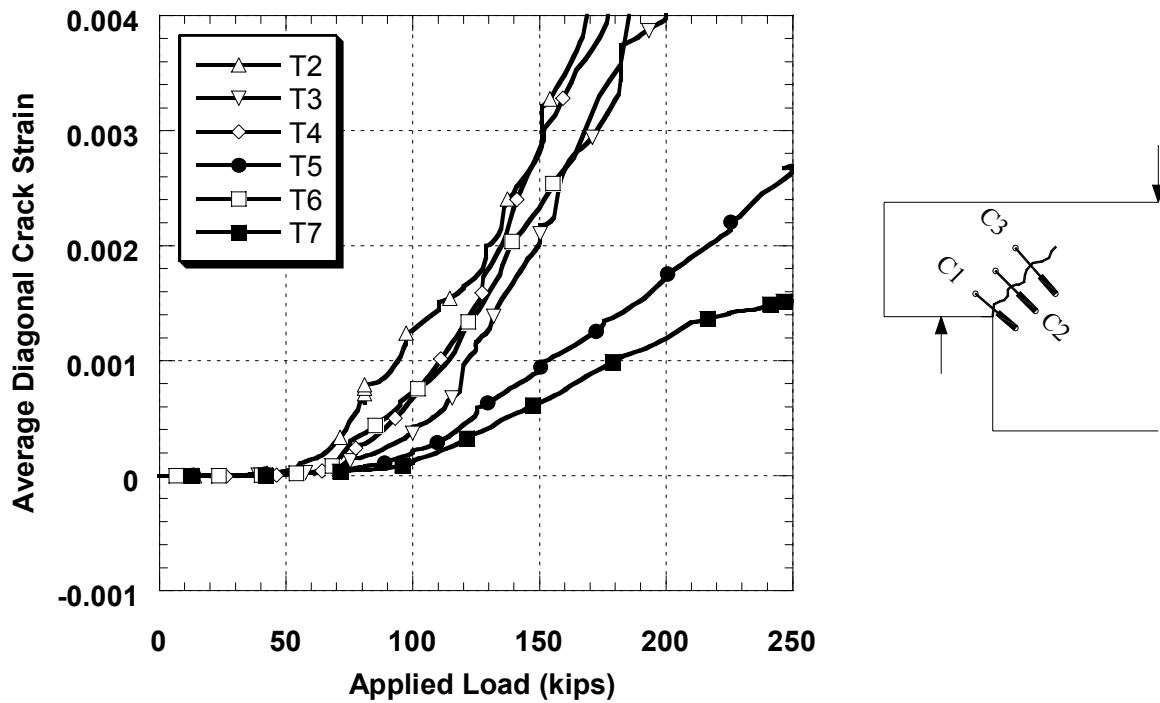


Fig. 3.8 Average Crack Strain of Specimen T2-T7

3.3.1 Effect of Diagonal Reinforcement

Two groups of curves can clearly be observed in Fig. 3.8. The first group of four curves were measured from specimens *without* diagonal bars (T2, T3, T4, and T6), while the second group of two curves were measured from specimens *with* diagonal bars (T5 and T7). Comparison of these two groups of curves indicates that the diagonal reinforcement plays the most significant role in reducing the crack widths.

Let us compare the average diagonal crack strain curves of Specimen T2 (without diagonal bars) and T5 (with diagonal bars). These two specimens have the same amount of hanger and flexural reinforcement. It can be seen that Specimen T2 without diagonal bars has the largest average diagonal crack strain at service load stage. In Specimen T5 with only three diagonal bars, the average diagonal crack strain is reduced very

drastically. This means that diagonal reinforcement is indeed the most effective means to control diagonal crack width.

Let us now compare the average diagonal crack strain curves of Specimen T5 and T7. Specimen 7 is identical to Specimen 5, except that the diagonal bars were increased from 3 to 5. Fig. 3.8 shows that although specimen T7 has somewhat smaller crack widths, the efficiency of using a large amount of diagonal reinforcement may be reduced.

The observation that diagonal steel is very efficient in reducing crack widths is also theoretically sound. This is because the diagonal bars are oriented in the direction normal to the direction of the crack. Since the direction of the crack is perpendicular to the direction of principal tensile stress, the direction of diagonal bars is, therefore, parallel to the direction of the principal tensile stress. It is well established that steel bars which are parallel to the principal tensile stress can control the cracks most effectively.

3.3.2 Effect of Hanger Reinforcement

The effect of hanger reinforcement in reducing the crack width can be seen from Fig. 3.8 by comparing the diagonal crack strain curves of Specimen T2 and T3. These two specimens are identical in reinforcement arrangement, except that Specimen T2 has 3 No. 6 hanger bars, while Specimen T3 has 5. Fig. 3.8 shows that the curves for Specimen T3 is lower than that of Specimen T2, meaning that hanger steel is effective in reducing crack width.

3.3.3 Effect of Flexural Reinforcement

The effectiveness of the flexural reinforcement could not be clearly discerned because this variable is not isolated in this test series. However, it is possible to infer from a comparison of Specimens T4 and T6 that the flexural steel is almost as effective as the hanger steel. Specimen T4 has 3 hanger steel bars and 5 flexural steel bars, while

Specimen T6 has 5 hanger steel bars and 3 flexural steel bars. The cracking behaviors of these two specimens are quite similar.

3.3.4 Effect of Shear-friction Reinforcement

The effectiveness of shear-friction reinforcement can be observed by comparing the crack strain curves of Specimen T3 vs. T6. Specimens T3 and T6 have the same amount of hanger and flexural reinforcement. The only difference is that T3 has two No. 6 shear-friction steel bars while T6 has none. It is interesting to observe that the crack strain of Specimen T3 at its service load (111-143 kips) is larger than the crack strain of Specimen T6 at its service load (104-124 kips). In other words, shear-friction reinforcement is not effective in reducing the crack width at service load.

In conclusion, diagonal reinforcement is very effective in increasing the ultimate strength and in controlling the crack widths at service load. In contrast, shear-friction reinforcement is only moderately effective in increasing the ultimate strength of the specimen, and is not very effective in controlling cracks at service load. Therefore, elimination of designs using shear-friction reinforcement, in favor of designs using diagonal reinforcement, is indicated.

3.4 Strain Measurement from SR4 Strain Gauges

Fig. 3.9 indicates the location of 6-mm SR4 strain gauges. Four gauges were attached to one of each of the hanger, flexural, diagonal, and shear-friction steel bars near the re-entrant corners of the specimen. The gauges are spaced at 4-inch center-to-center.

Strain distributions on the hanger, flexural, diagonal, and shear-friction steel bars in all six specimens at the midpoint of service load range are shown in Fig. 3.10 (a) to (f). The horizontal axis indicates the locations of the SR4 strain gauges indicated in Fig. 3.9. The vertical axis indicates the strain values of hanger or flexural steel bars measured by

SR4 gauges. At this load stage, there is generally only one crack at each re-entrant corner, and the two inside strains (measured at locations 2 and 3) straddling the crack are significantly larger than the two strains measured on the outside locations (1 and 4). It is interesting to observe that although the service load is at least 0.6 times the yield load, the maximum strain for each specimen at service load is somewhat less than 0.6 times the yield strain of 0.0022.

Strain vs. location diagrams are also given in Fig. 3.11 (a) to (f) at the first yield load. It can be seen that the maximum strain of each specimen at locations 2 or 3 near the crack reaches at least the yield strain of 0.0022 (64,000 psi/29,000,000 psi) of steel bars. The distribution of strains along the bars at the crack region, in which additional cracks have formed, is much more uniform than that at service load.

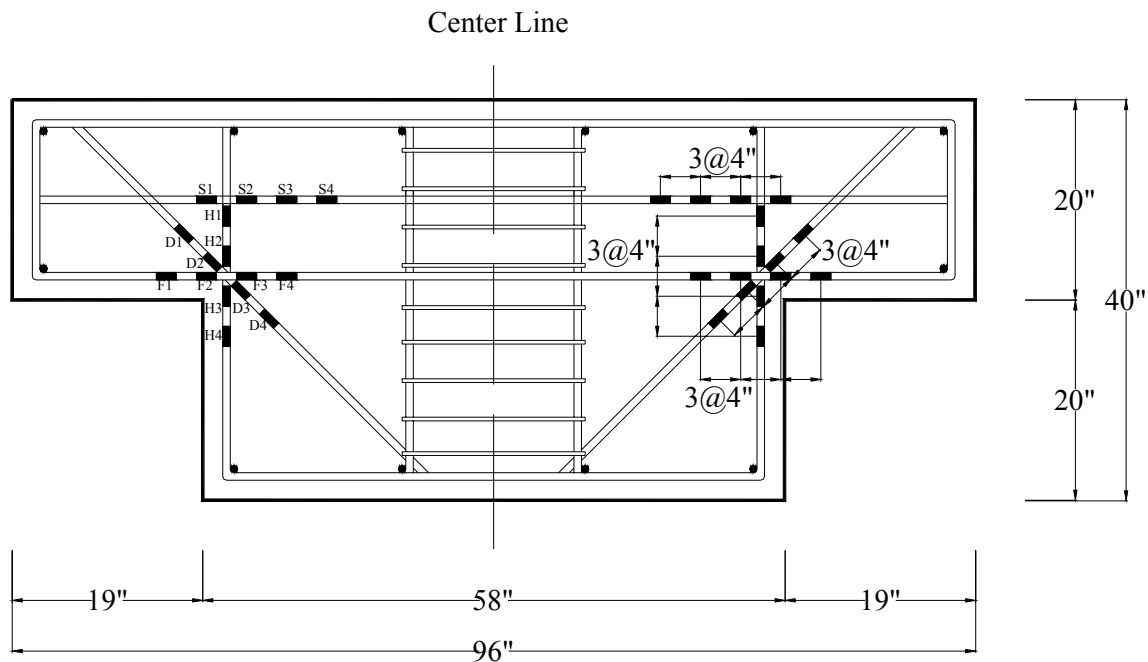


Fig. 3.9 Locations of All SR4 Strain Gauges on Steel Reinforcement

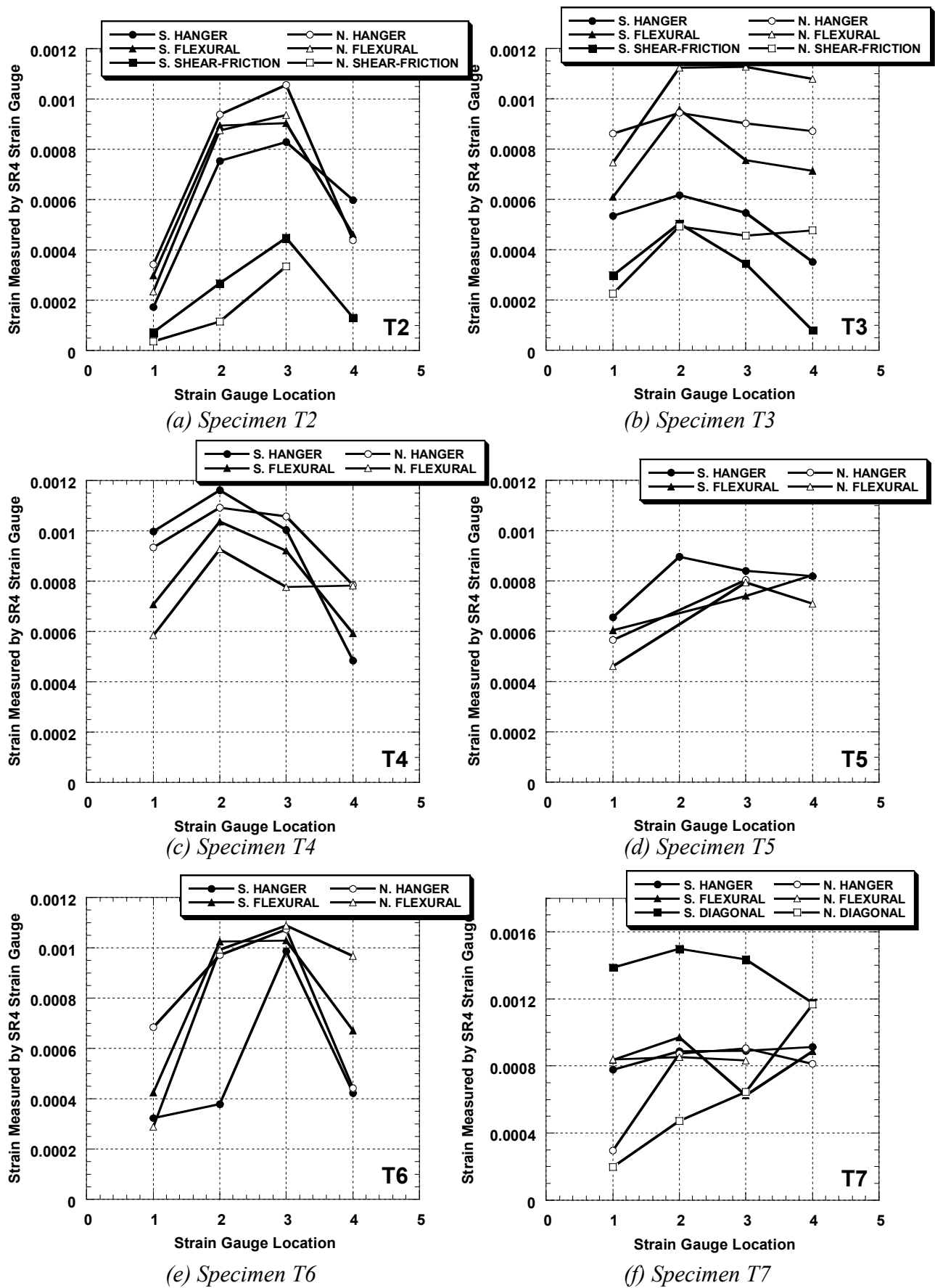


Fig. 3.10 Strain Distribution of Steel Bars at Mid-point of Service Load Range

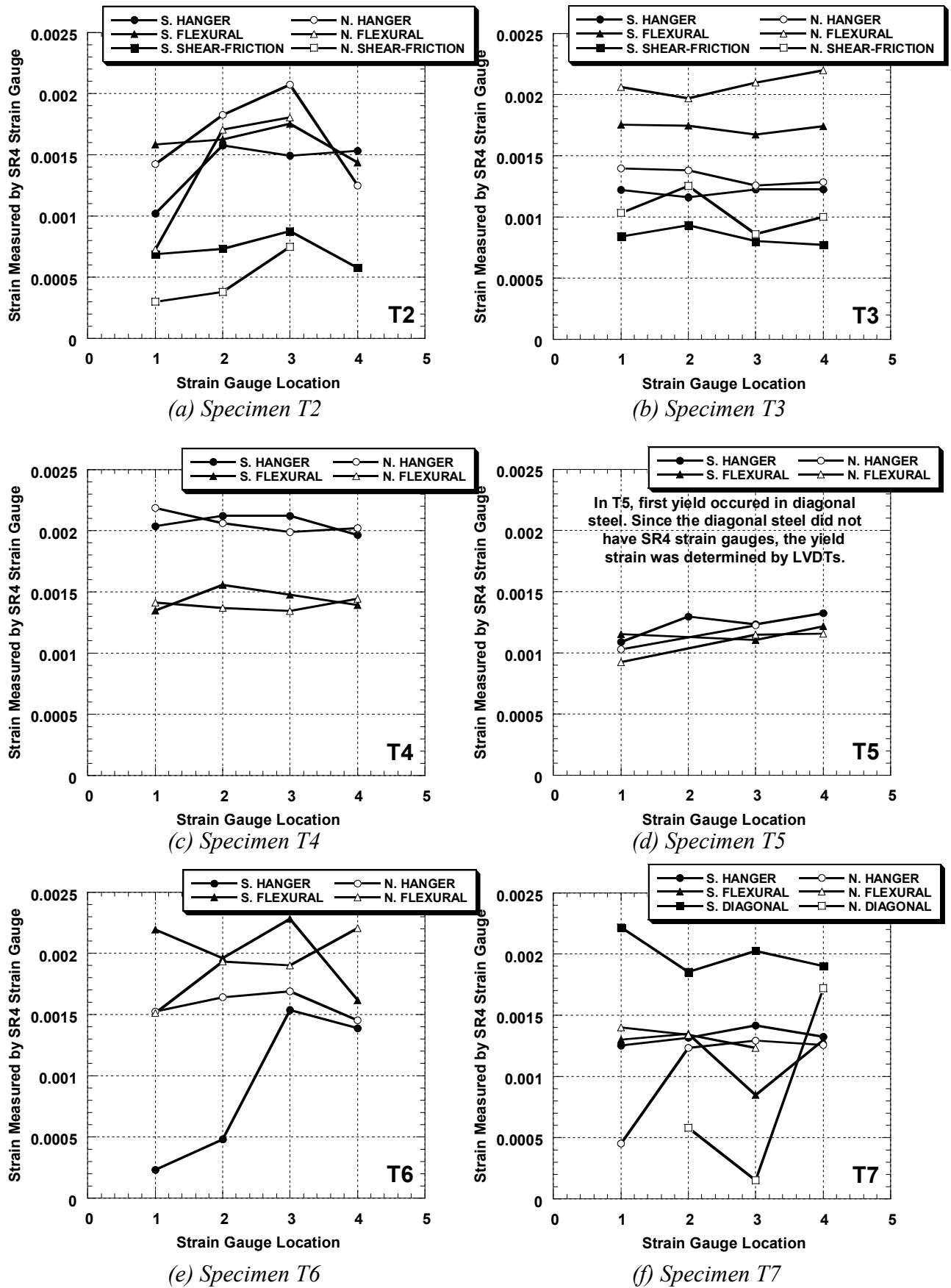


Fig. 3.11 Strain Distribution of Steel Bars at First Yield

3.5. Direct Measurements of Crack Widths Using Microscopes

Fig. 3.12 shows a diagonal crack at the re-entrant corner at the *west* end of specimen T4 on the *north* face. At three locations on the diagonal crack (designated by lines 1, 2, and 3), measurements were made using a hand-held microscope at every 20-25 kips interval of total applied load. The precision of the microscope is indicated by the smallest 0.001 in. division. At this same *west* end of specimen on the *south* face, three LVDTs (SC1, SC2, and SC3) measure the strains (over a gauge length of 9.5 in.) of this same diagonal crack at the corresponding 3 locations. All strain data measured at the three locations by LVDTs are then converted to crack widths and compared to the values measured by the hand-held microscopes as shown in Table 3.1. Comparison is also made at the *east* end of the specimen at the three locations as shown in Table 3.2. These comparisons at the six locations are also shown graphically in Fig. 3.13 (a) to (f).

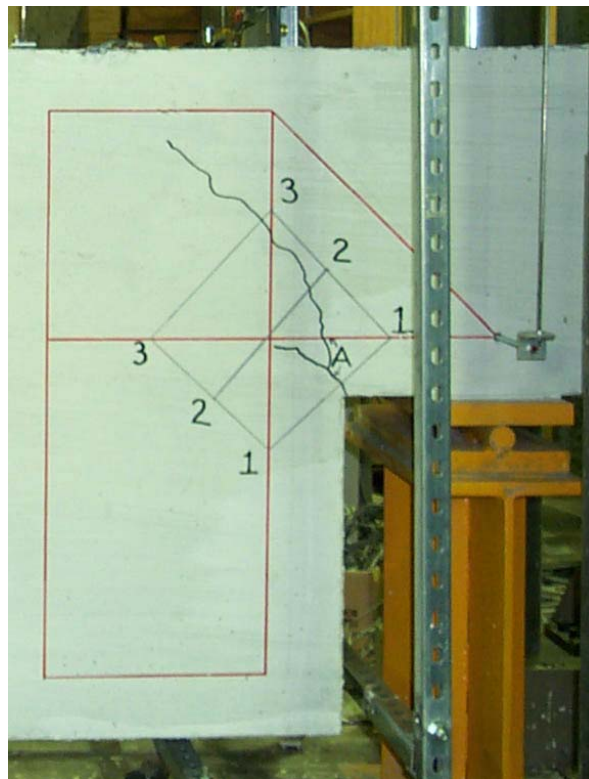


Fig. 3.12 Diagonal Crack Region and the three Locations to Measure Crack Widths

Fig. 3.13 (a) to (f) show that the crack widths at the six locations measured by LVDTs using a gauge length of 9.5 in. compare very well with the crack widths measured directly using hand-held microscopes at the service load range. After the first yielding, however, crack widths made by these two types of measurements could diverge. This observation can be explained as follows: At the service load range, only one diagonal crack appears within the 9.5 in. gauge lengths. After the first yield, however, additional cracks appear within the gauge lengths. In this higher load stage an LVDT could measure the total crack widths of two or more cracks, while a microscope still records the crack width of one crack.

The average crack widths at the six locations of specimen T4 (without diagonal bars) measured by LVDTs and by hand-held microscopes are compared in Fig. 3.14. It can be seen the agreement between the two methods of measurement is excellent at the service load range. Beyond the first yield, the agreement is still acceptable. The average crack widths at the six locations of specimen T5 (with diagonal bars) measured by LVDTs and by hand-held microscopes at the service load are compared in Fig. 3.15. Again, the agreement between the two methods of measurement is excellent. In short, the two methods of measurements are applicable to specimens with or without diagonal bars. Because of these close agreements, the crack width measured by the LVDTs will be used in the formulation of the CASTM method of crack width prediction (4.2 and 4.3).

Table 3.1 Comparison of Crack Widths (in.) Measured by Microscope and by LVDTs
(West End of T4: North Microscope vs. South LVDTs)

	Microscope		Microscope		Microscope	
Load (kips)	North	LVDT	North	LVDT	North	LVDT
	Location 1	SC1	Location 2	SC2	Location 3	SC3
75	0.005	0.003	0.003	0.001	0.003	0.000
100	0.015	0.010	0.008	0.005	0.007	0.001
125	0.026	0.017	0.017	0.011	0.015	0.003
150	0.035	0.034	0.026	0.022	0.018	0.009
175	0.037	0.052	0.029	0.028	0.024	0.012
200	0.051	0.069	0.034	0.036	0.032	0.016
210	0.058	0.074	0.043	0.038	0.034	0.018
220	0.070	0.095	0.047	0.049	0.048	0.026
240	0.098	0.136	0.066	0.073	0.073	0.044
243	0.108	0.161	0.083	0.089	0.083	0.056
242	0.110	0.186	0.095	0.101	0.084	0.066
245	0.115	0.256	0.100	0.107	0.079	0.071
250	0.143	0.341	0.110	0.115	0.114	0.077
255	0.224	0.425	0.132	0.131	0.124	0.088
252	0.276	0.426	0.220	0.170	0.195	0.102

Table 3.2 Comparison of Crack Widths (in.) Measured by Microscope and by LVDTs
(East End of T2: South Microscope vs. North LVDTs)

	Microscope		Microscope		Microscope	
Load (kips)	South	LVDT	South	LVDT	South	LVDT
	@ 1	NC1	@ 2	NC2	@ 3	NC3
75	0.004	0.003	0.002	0.012	0.001	0.000
100	0.012	0.012	0.005	0.008	0.004	0.003
125	0.021	0.026	0.012	0.019	0.006	0.008
150	0.033	0.043	0.013	0.034	0.015	0.016
175	0.053	0.057	0.045	0.047	0.021	0.022
200	0.060	0.079	0.047	0.067	0.026	0.031
210	0.072	0.081	0.055	0.070	0.030	0.033
220	0.081	0.089	0.047	0.077	0.036	0.038
240	0.103	0.111	0.075	0.096	0.050	0.053
243	0.095	0.126	0.090	0.110	0.060	0.063
242	0.103	0.134	0.084	0.117	0.065	0.068
245	0.103	0.139	0.099	0.121	0.060	0.072
250	0.137	0.163	0.121	0.142	0.090	0.087
255	0.170	0.200	0.208	0.174	0.100	0.109
252	0.310	0.251	0.165	0.218	0.125	0.119

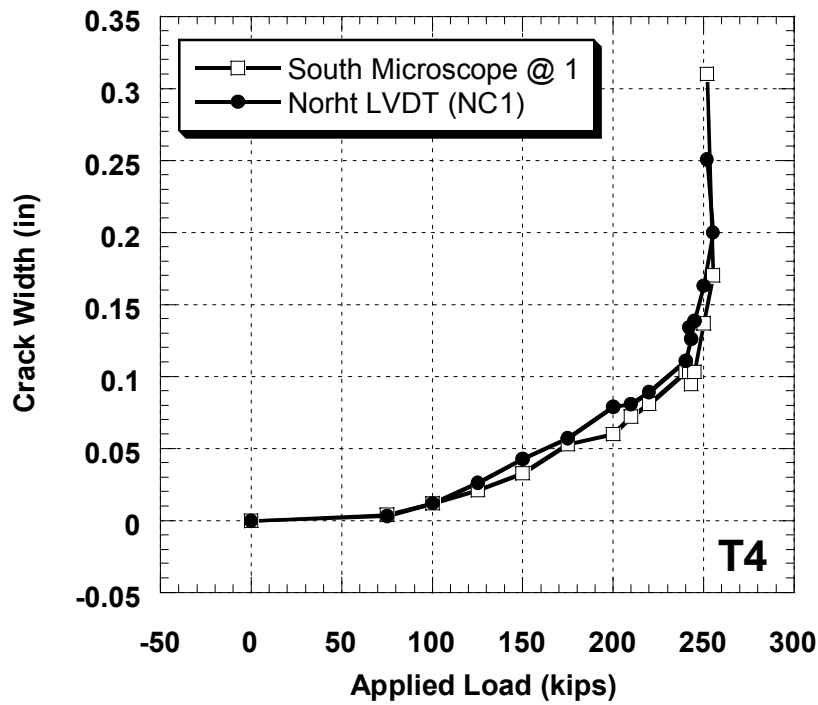


Fig. 3.13 (a) Comparison of Measurements made by Microscope and LVDT at Location 1 at West End of Specimen T4

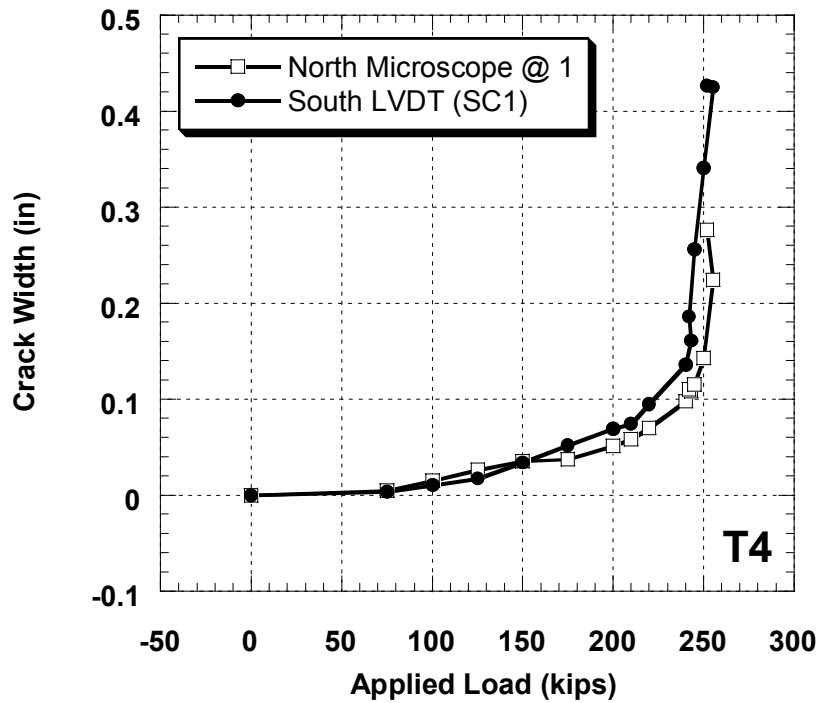


Fig. 3.13 (b) Comparison of Measurements made by Microscope and LVDT at Location 1 at East End of Specimen T4

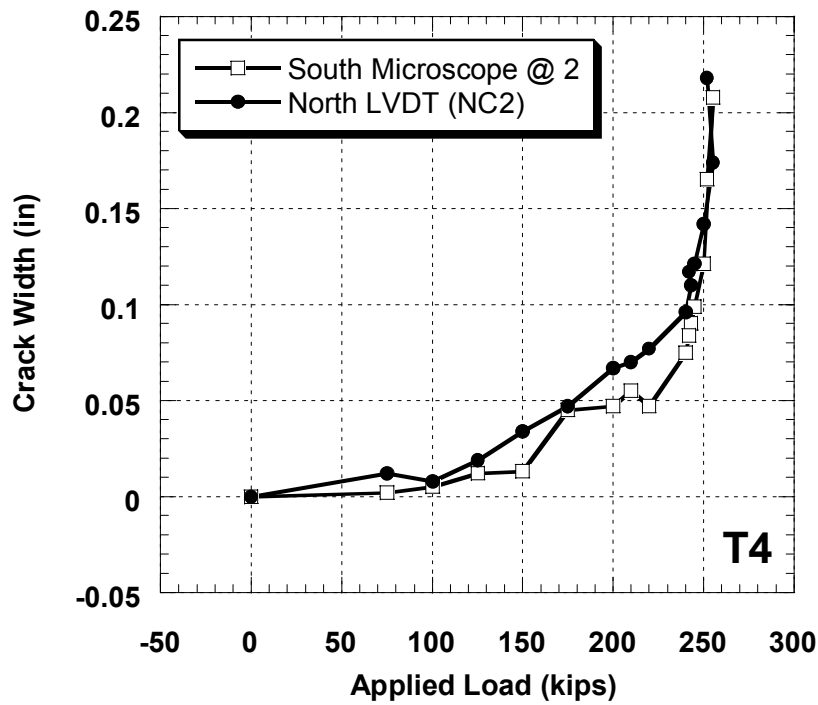


Fig. 3.13 (c) Comparison of Measurements made by Microscope and LVDT at Location 2 at West End of Specimen T4

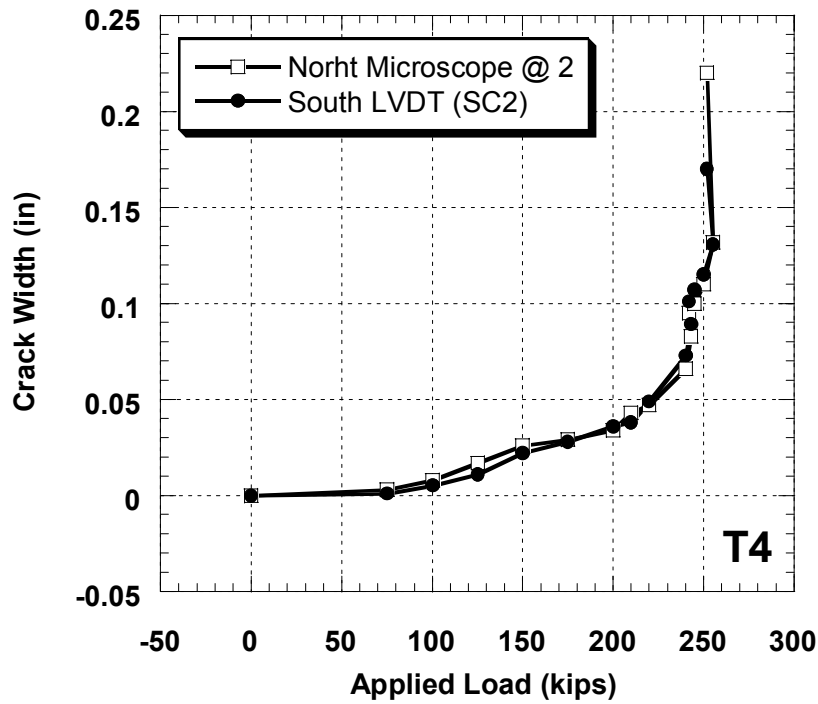


Fig. 3.13 (d) Comparison of Measurements made by Microscope and LVDT at Location 2 at East End of Specimen T4

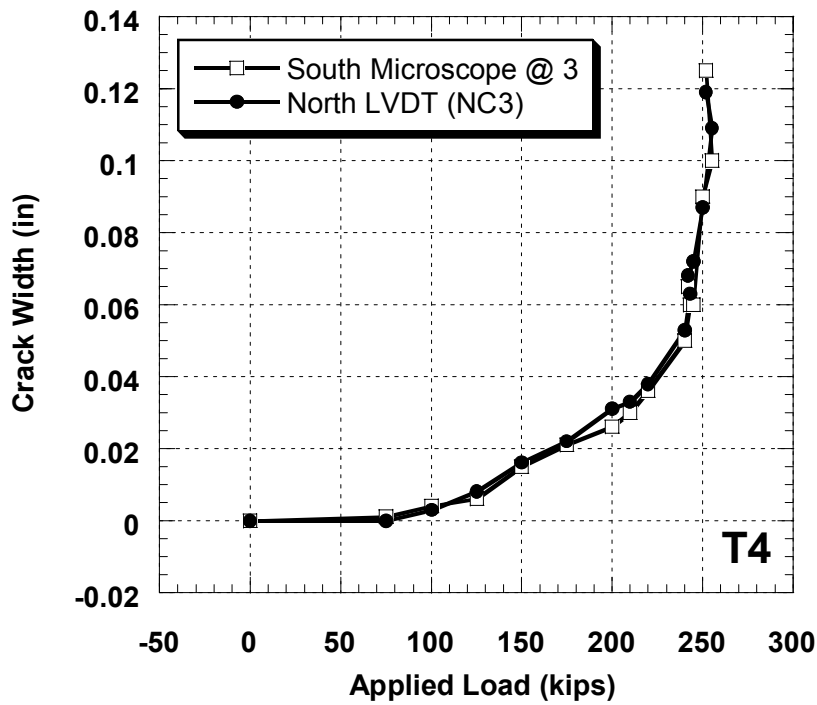


Fig. 3.13 (e) Comparison of Measurements made by Microscope and LVDT at Location 3 at West End of Specimen T4

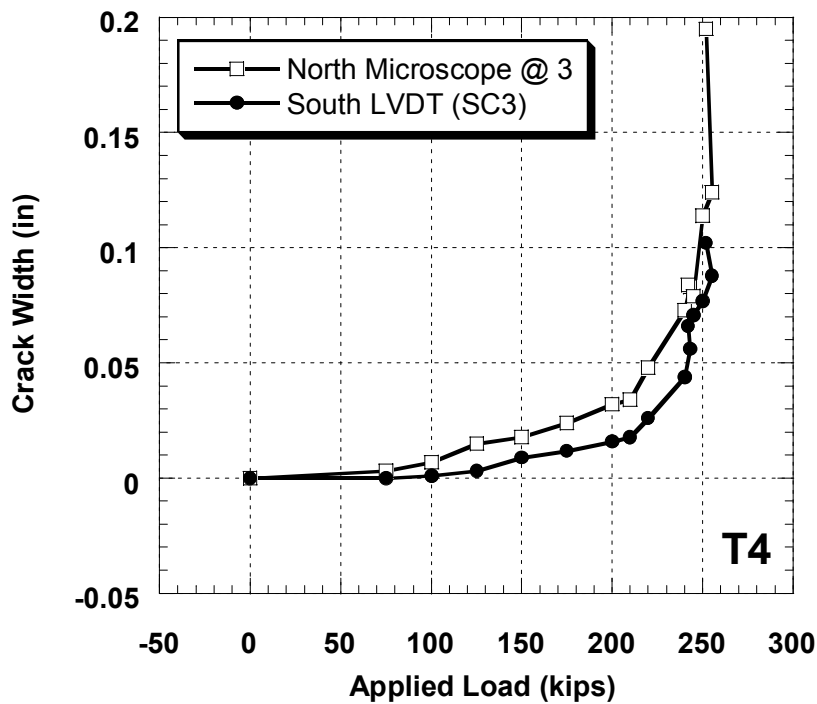


Fig. 3.13 (f) Comparison of Measurements made by Microscope and LVDT at Location 3 at East End of Specimen T4

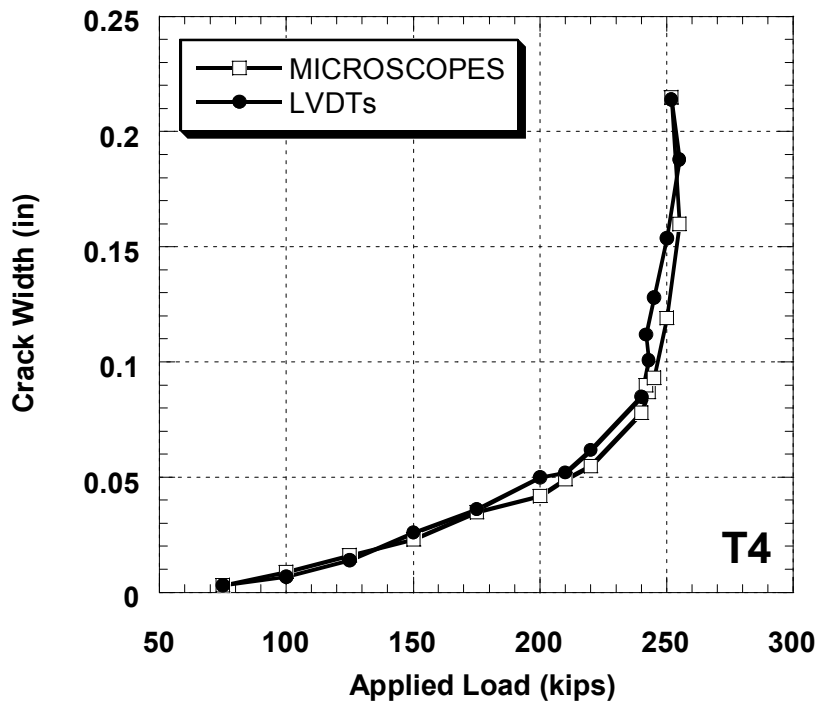


Fig. 3.14 Comparison of Average Crack Width Measurements by Microscopes and LVDTs for Specimen T4

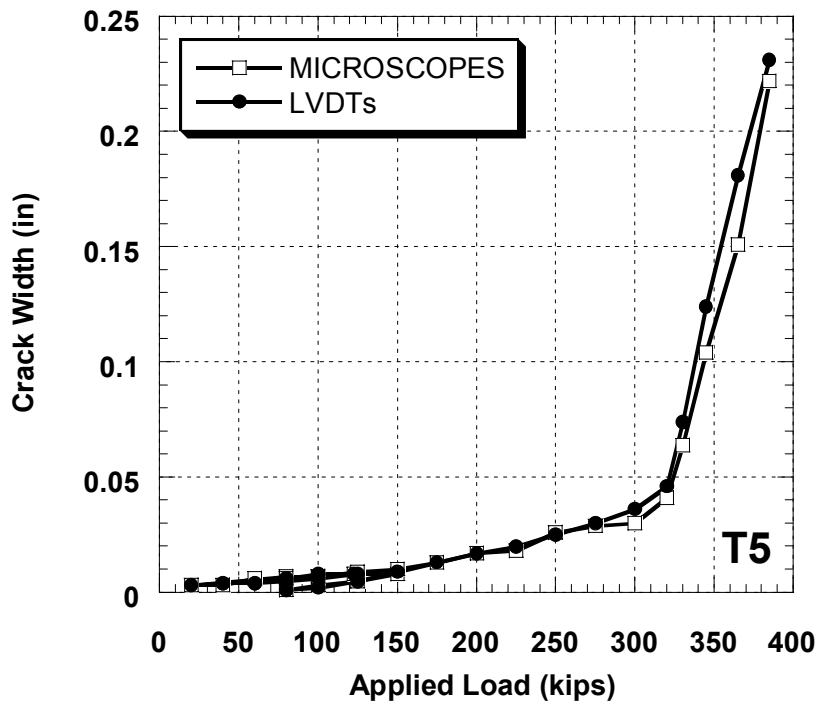


Fig. 3.15 Comparison of Average Crack Width Measurements by Microscopes and LVDTs for Specimen T5

4. COMPATIBILITY-AIDED STRUT-AND-TIE MODEL (CASTM)

4.1 Introduction to CASTM

In structures such as inverted ‘T’ bent caps, dapped ends, corbels, etc., large diagonal cracks often develop at the re-entrant corners. The re-entrant corner is a type of D-region which has very complex distribution of stresses and strains, and is, therefore, very difficult to analyze. An efficient method to evaluate the diagonal crack widths is to model such a region as a truss composed of steel bars as tension ties and concrete along cracks as compression struts.

This strut-and-tie model is currently being widely used in the ultimate strength design of concrete structures (Schlaich et als, 1985). In this type of modelling, only the equilibrium condition at ultimate load stage needs to be satisfied. In our research on the serviceability of concrete structures, however, we propose to apply this strut-and-tie model to the evaluation of crack widths by taking into account the compatibility condition. This **Compatibility-Aided Strut-and-Tie Model (CASTM)**, which satisfies both the equilibrium of forces and the compatibility of deformations, is not only conceptually clear, but is quite simple for practical application.

The proposed CASTM is intended for predicting the diagonal crack widths at re-entrant corners of inverted ‘T’ bent caps both *with* and *without* diagonal steel bars. This CASTM is substantiated by the tests of seven 2-D specimens, BPC1, T2, T3, T4, T5, T6, and T7. Because the CASTM utilize statically determinate trusses, the model is easy to understand and to analyze. The resulting crack width design equations have clear physical meaning, and can easily be accepted by bridge engineers.

4.2 CASTM without diagonal bar

4.2.1 Strut-and-tie model

Fig. 4.1 shows the first type of CASTM without diagonal steel bars. The member forces for hanger bar H and flexure bar F can easily be determined by static equilibrium as shown below:

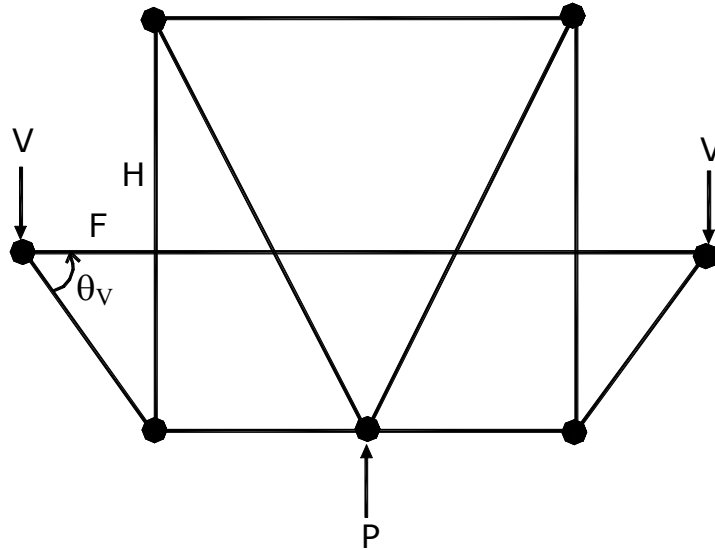


Fig. 4.1 CASTM Without Diagonal Bar

$$H = V, \quad (4-1)$$

$$F = V \cot \theta_v \quad (4-2)$$

For the 2-D specimens designed for this research, $\theta_v = 53.28^\circ$ and $F = 0.75 V$.

4.2.2 Diagonal Crack Strain Contributed by Hanger (Vertical) and Flexural (Horizontal) Steel Bars

Test observation of diagonal cracks between the cantilever ledge and the web at service load shows that there is only one crack or one dominant crack at the service load range and the diagonal crack width is primarily a function of the strains in the hanger steel bar H and the flexural steel bar F (Fig. 4.1). The diagonal crack strain can be directly related to the strains

measured in the hanger steel and flexural steel as shown in Fig. 4.2. Let's define the gauge lengths for hanger steel bar and flexural steel bars as L_H and L_F , respectively, and the gauge strains for hanger and flexural steel bars as ϵ_H and ϵ_F , respectively. Using the compatibility condition and assuming the diagonal crack to be oriented at about 45 degree, the diagonal crack width w can be closely approximated as follows:

$$w = \sqrt{(\epsilon_H L_H)^2 + (\epsilon_F L_F)^2} \quad (4-3)$$

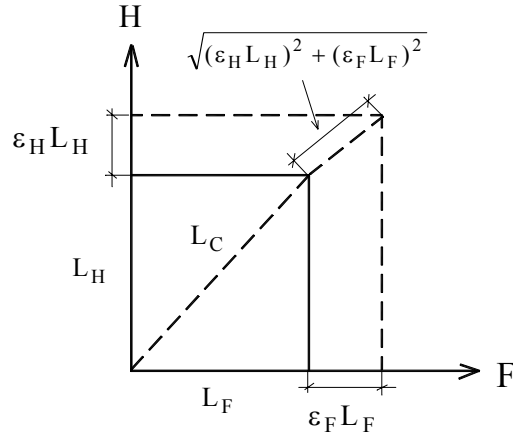


Fig. 4.2 Determination of Diagonal Crack Strain

Since the gauge length for the diagonal strain is L_c , then the diagonal cracking strain ϵ_c is

$$\epsilon_c = \frac{w}{L_c} \quad (4-4)$$

Substituting Eq. (4-3) into Eq. (4-4) gives

$$\varepsilon_c = \frac{\sqrt{(\varepsilon_H L_H)^2 + (\varepsilon_F L_F)^2}}{L_c} \quad (4-5)$$

In the tests of the seven 2-D specimens, the hanger bar gauge length L'_H and flexural bar gauge length L'_F were both taken as 14 in., and the gauge length for diagonal crack strain L'_C was 9.5 in. Substituting these gauge length values into Eq. (4-5) gives the diagonal crack strain as

$$\varepsilon'_c = 1.474 \sqrt{\varepsilon'_H{}^2 + \varepsilon'_F{}^2} \quad (4-6)$$

where ε'_c , ε'_H and ε'_F are the strains based on our LVDT measurements.

Fig. 4.3 compares two methods of obtaining the diagonal crack strains for the six 2-D specimens reported in Section 2. Method 1 is to measure the diagonal crack strain directly from the three diagonal LVDTs (C1 – C3) located in the diagonal crack region as indicated in Fig. 2.4. Method 2 is to measure the vertical strain (ε'_H for hanger steel) from the vertical LVDTs (V4) and the horizontal strain (ε'_F for flexural steel) from the horizontal LVDT (H4), and then to calculate the diagonal crack strains (ε'_c in diagonal direction) by Eq. (4-6). It can be seen that the two curves, which represent these two methods of measurements, agree very well. This agreement means that Eq. (4-6), and therefore, Eqs. (4-4) and (4-5), are valid throughout the whole loading history.

The six specimens (T1 to T7) in Fig. 4.3 include two specimens with diagonal bars (T5 and T7). Since Method 1 and Method 2 also agree very well for these two specimens, Eqs. (4-4) to (4-6) are valid not only for specimens *without* diagonal bars, but also for specimens *with* diagonal bars.

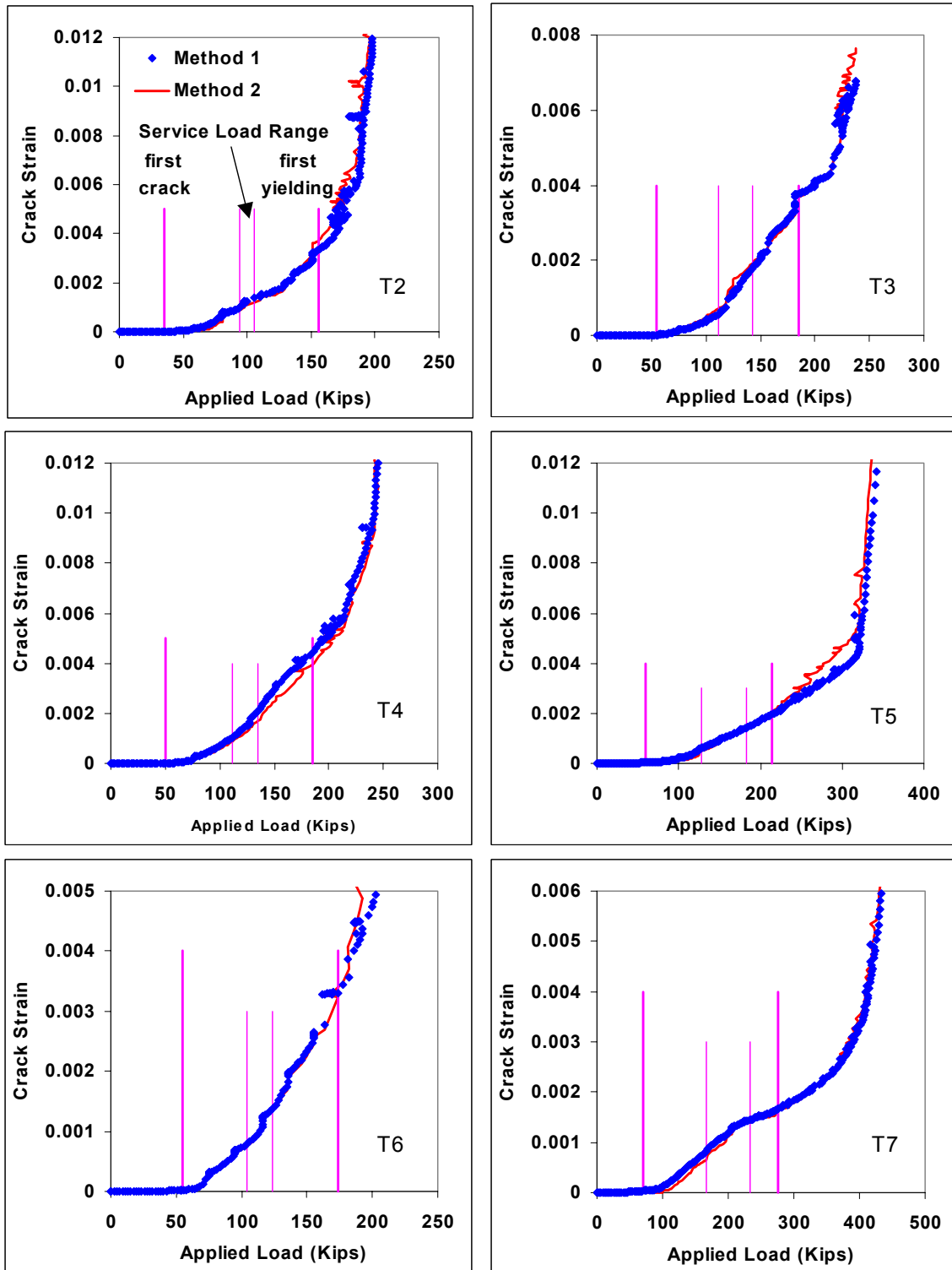


Fig. 4.3 Comparison of Diagonal Crack Strains Measured by Method 1 and Method 2

4.2.3 Member Stiffness for CASTM Strains

The service load stage is difficult to define because the yielding sequences of hanger, flexural and diagonal bars are different for different reinforcement design. For convenience, the service load stage is defined as a range from 60% of the first yield load to 60% of the last yield load. In the case where none of the steel bars in the three directions yielded, the ultimate load will be used as the last yield load.

The service load ranges for the six specimens T2 to T7 as defined above are indicated in Fig. 4.3. It can be seen that each service load range is located in the post-cracking elastic range between the cracking load and the first yield load. In this post-cracking elastic range, the steel bars and the concrete are expected to behave in a linear manner and the axial load stiffness of the truss members can be taken as a constant.

The strain for tie member H in specimens without diagonal steel bars can be calculated as follows:

$$\varepsilon_H = \frac{F_H}{E_H A_H} \quad (4-7)$$

where the member force F_H can be determined from equilibrium to be $F_H = V$. The stiffness $E_H A_H$ is the sum of the stiffness of steel bars ($E_{SH} A_{SH}$) and the stiffness of concrete surrounding the steel bars ($E_{CH} A_{CH}$):

$$E_H A_H = E_{SH} A_{SH} + E_{CH} A_{CH} \quad (4-8)$$

In Eq. (4-8) E_{SH} is the elastic modulus of steel equal to 2,900,000 psi, and A_{SH} is the area of steel bars for member H. The area of concrete for each steel bar can be taken as a square as shown in Fig. 4.4. The area of concrete A_{CH} is the sum of all the individual concrete areas for all the steel bars.

The elastic modulus of concrete, E_{CH} , is calculated for two cases. For the case of compression struts, the modulus of elasticity specified by the ACI Code ($E_c = 57,000\sqrt{f'_c}$) is used. For the case of tension ties, the constitutive relationship of cracked concrete proposed by Belarbi and Hsu (1994) is used to calculate the modulus of concrete, E_{CH} . Since E_{CH} after

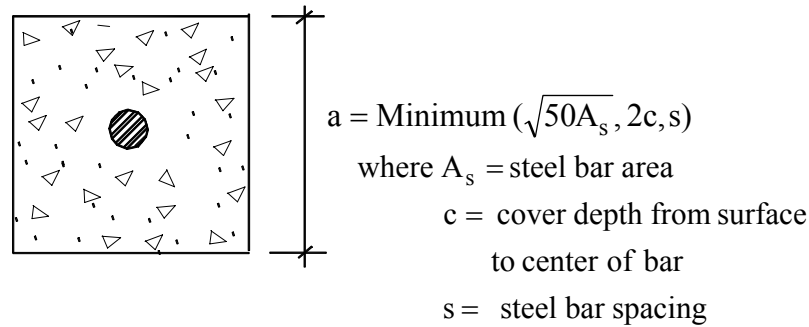


Fig. 4.4 Determination of Concrete Area Surrounding a Steel Bar

cracking is much smaller than the compressive modulus of concrete, the tensile strain used to calculate the concrete modulus at service load can be taken as a constant. Based on the test results, an average tensile strain of 0.0008 is proposed which gives the modulus as follows:

$$E_{CH} = 3.75 \sqrt{f'_c} \frac{\left(\frac{0.00008}{0.0008}\right)^{0.4}}{0.0008} = 1866 \sqrt{f'_c} \text{ psi. } (f'_c \text{ and } \sqrt{f'_c} \text{ are in psi})$$

The strain for tie member F (flexural steel) in specimens without diagonal steel bars can be treated in the same way.

4.2.4 Calibration of CASTM Gauge Length

Assuming the CASTM gauge lengths for hanger and flexural bar strains to be the same, then these gauge lengths can be calibrated by experiments based on Eq. (4-5) or (4-6) as follows:

$$L_{HF} = \frac{L'_c \varepsilon'_c}{\sqrt{\varepsilon_H^2 + \varepsilon_F^2}} \quad (4-9)$$

where

L_{HF} = CASTM gauge length for calculated hanger and flexural steel strains.

L'_c = gauge length used in experiments for diagonal crack strain (9.5 in.).

ε'_c = diagonal crack strain measured by diagonal LVDTs in experiments.

ε_H = Strain in hanger steel calculated by Eq. (4-7) using CASTM truss forces.

ε_F = Strain in flexural steel calculated by Eq. (4-7) using CASTM truss forces, but replacing the subscript H by F.

After the CASTM gauge lengths are obtained, the diagonal crack width w can be calculated as follows:

$$w = L_{HF} \sqrt{\varepsilon_H^2 + \varepsilon_F^2} \quad (4-10)$$

The CASTM gauge lengths L_{HF} calculated by Eq. (4-9) for all the specimens are shown in Fig. 4.5. It can be seen that the average gauge length increase with the strain $\varepsilon_{HF} = \sqrt{\varepsilon_H^2 + \varepsilon_F^2}$. For the convenience of design, a simple linear equation is used to represent all the curves as follows:

$$L_{HF} = 9500\varepsilon_{HF} - 3.0 \quad (4-11)$$

Fig. 4.5 shows that the range of CASTM gauge lengths for the six specimens varies from 7 in. to 12 in. The average CASTM gauge length of 9.5 in. is identical to the actual gauge length

selected for the diagonal cracks in the test specimens. This means that our choice of gauge length for the diagonal cracks turns out to be very appropriate. The success in the calibration of the CASTM gauge length is due partly to the judicious choices of the gauge lengths for the diagonal cracks.

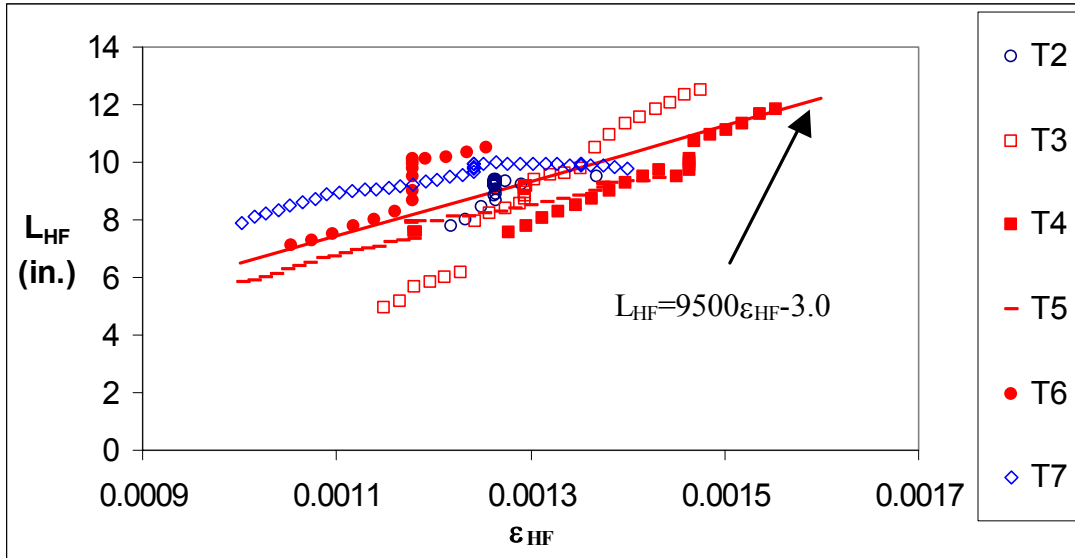


Fig. 4.5 Calibration of CASTM gauge lengths

4.2.5 Design Criteria of CASTM without Diagonal Bars

Now that the CASTM gauge length L_{HF} is calibrated, the diagonal crack width w can be predicted by the CASTM as follows:

$$w = L_{HF} \varepsilon_{HF} \quad (4-12)$$

where

w = predicted diagonal crack width (in.)

L_{HF} = CASTM gauge length for calculated hanger and flexural steel strains

= $9500 \varepsilon_{HF} - 3.0$ (in.)

ε_{HF} = diagonal crack strain calculated by hanger and flexural strains = $\sqrt{\varepsilon_H^2 + \varepsilon_F^2}$

ε_H = hanger strain or strain in the vertical direction = $\frac{V}{E_S A_{SH} + E_C A_{CH}}$

ε_F = flexural strain or strain in the horizontal direction = $\frac{V \cot \theta_V}{E_S A_{SF} + E_C A_{CF}}$

V = applied service load at each ledge (in pounds)

θ_V = Angle between flexural steel bars and the diagonal strut at the point of load V

A_{SH} = total cross-sectional area of hanger reinforcement at each ledge (in.²)

A_{CH} = total effective concrete area surrounding hanger reinforcement (in.²)

A_{SF} = total cross-sectional area of flexural reinforcement at each ledge (in.²)

A_{CF} = total effective concrete area surrounding flexural reinforcement (in.²)

E_S = 29,000,000 psi

E_C = 57,000 $\sqrt{f'_C}$ (psi) for compression and 1,866 $\sqrt{f'_C}$ (psi) for tension

f'_C = concrete cylinder compressive strength (psi)

4.3 CASTM with diagonal bars

4.3.1 Two Sub-Trusses

Fig. 4.6 shows the second type of CASTM with diagonal steel bars. The combined truss with hanger steel, flexural steel and diagonal steel is statically *indeterminate*. This combined truss can be separated into two sub-trusses, which are statically *determinate*. The first sub-truss is constituted using the hanger and flexural steel bars; while the second sub-truss involves the diagonal bar. The relative magnitude of the loads carried by the two sub-trusses can be determined by their relative stiffnesses, which can be calculated by virtual work.

The member forces for hanger bar H, flexure bar F and diagonal bar D can easily be determined by static equilibrium as shown below:

$$H = (1-B)V, \quad (4-13)$$

$$F = (1-B)V \cot \theta_V. \quad (4-14)$$

$$D = \frac{BV}{\cos \theta_D} \quad (4-15)$$

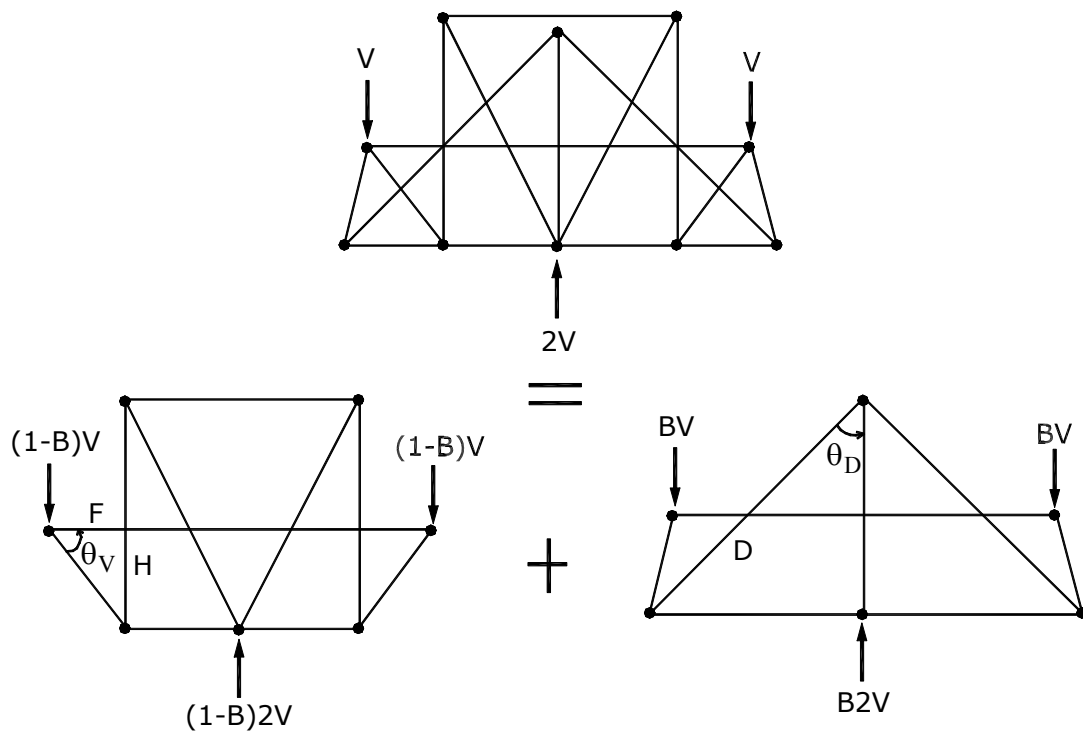


Fig. 4.6 CASTM with Diagonal Bars Simulating the Test Specimens

For the 2-D specimens designed for this research, $\theta_V = 53.28^\circ$ and $\theta_D = 45^\circ$. Therefore, $H = (1-B)V$, $F = 0.75(1-B)V$, and $D = 1.414BV$.

The symbol B in Eqs. (4-13) to (4-15) is the distribution factor which determine the percentages of loads carried by the two sub-trusses. If the second sub-truss with the diagonal bar D is assumed to carry B percentage, then the first sub-trusses must carry $(1-B)$ percentage. After an exhaustive analysis of various trusses with various distributions of hanger steel, flexural steel and diagonal steel, the following equation is proposed:

$$B = \frac{A_{SD}}{A_{SH} + 0.5A_{SF} + A_{SD}} \quad (4-16)$$

where

A_{SD} = Diagonal Steel Bar Area,

A_{SH} = Hanger Steel Bar Area,

A_{SF} = Flexural Steel Bar Area.

4.3.2 Determination of Distribution factor B

The distribution factor B was derived from the relative stiffness of the two sub-trusses, which can be calculated by virtual work analysis. A specimen with 3 hanger steel bars, 2 flexural steel bars and 4 diagonal bars is used as an example to calculate the B factor. The steel area ratios for this hypothetical specimen are: $A_{SF}/A_{SH} = 2/3 = 0.67$ and $A_{SD}/A_{SH} = 4/3 = 1.33$.

Table 4.1 assembles the geometric and material properties for the two sub-trusses. Table 4.2 shows the procedure to calculate the B factor. The calculation takes advantage of the symmetry of the two sub-trusses, so that only half of each sub-truss needs to be used in the calculation of the internal work. The members in half of each sub-truss are labeled in Fig. 4.7. For members that span the whole length of the sub-trusses, such as $H2$ and $H3$ in sub-truss 1 and

member H2 in sub-truss 2, only half their lengths will be used. For the vertical member V1 lying in the plane of symmetry, only half of its force needs to be taken into account. The deflection per pound (Δ_p) of a whole sub-truss is twice the deflection calculated by the half-truss. Finally, the stiffness of the sub-truss is the reciprocal of Δ_p . Table 4.2 reveals a very important observation, i.e., the three members, D2 (diagonal bars in sub-truss 2), V1 (hanger bars) and H2 (flexural bars) in sub-truss 1, have a predominant effect in the CASTM.

Table 4.3 compares the values obtained by virtual work analysis of the CASTM and the values calculated by Eqs. (4-16). The comparison includes a systematic variation of the two steel area ratios, A_{SF}/A_{SH} and A_{SD}/A_{SH} . Table 4.3 shows that the predictions of Eq. (4-16) match very well with the rigorous structural analysis based on virtual work method. The same comparison is illustrated by graphs in Fig. 4.8.

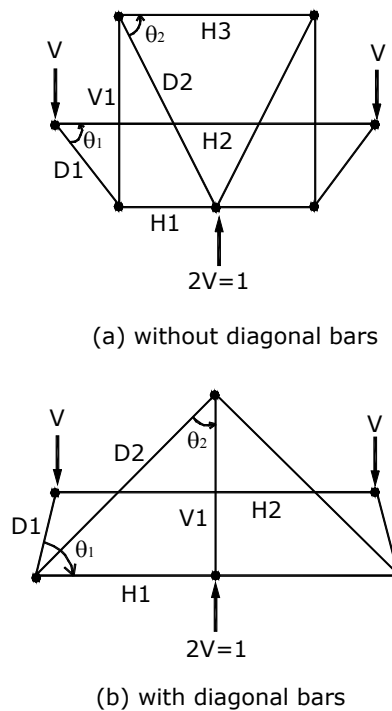


Fig. 4.7 Labels of Members in Two Sub-Trusses

Table 4.1, Parameters for Calculating Factor B

Sub-truss	θ_1 (degree)	θ_2 (degree)	V (lbs)	E_s (psi)	f'_c (psi)	E_{ct} (psi)	E_{cc} (psi)
1	53.28	62.95	0.5	29,000,000	5,000	131,955	4,030,509
2	75.74	45	0.5	29,000,000	5,000	131,955	4,030,509

Table 4.2, Example for Calculating Distribution Factor B

Sub-truss	Member	Virtual Force \bar{N}		Force N (lbs)	Length L (in.)	Concrete Area A_c (in. ²)	Steel Area A_s (in. ²)	$\frac{\bar{N}NL}{E_s A_s + E_c A_c}$ (in.x10 ⁻⁶)	
		Equilibrium formula	Value						
1	H1	$-V \cot \theta_1$	-0.3730	-0.3730	18.0	67.7	2.2	0.007	
	H2	$V \cot \theta_1$	0.3730	0.3730	29.4	45.1	0.88	0.130	
	H3	$V \cot \theta_2$	0.2553	0.2553	18.0	67.7	1.32	0.025	
	V1	V	0.5000	0.5000	35.3	67.7	1.32	0.187	
	D1	$-V / \sin \theta_1$	-0.6238	-0.6238	19.0	45.1	0	0.041	
	D2	$-V / \sin \theta_2$	-0.5614	-0.5614	37.8	67.7	0	0.044	
	Deflection (in.) per pound $\Delta_p = 2(\text{Sum})$								Sum = 0.434
Stiffness of Sub-truss 1 = $(1/\Delta_p) = 1.152 \times 10^6$ lbs/in.									
2	H1	$V / \tan \theta_1 - V \tan \theta_2$	-0.3729	-0.3729	33.25	85.5	0	0.013	
	H2	$-V \cot \theta_1$	-0.1271	-0.1271	29.38	85.5	0	0.001	
	V1	-2V	-1.0000	-0.5000	33.25	85.5	0	0.048	
	D1	$-V / \sin \theta_1$	-0.5159	-0.5159	16	85.5	0	0.012	
	D2	$V / \cos \theta_2$	0.7071	0.7071	47	85.5	1.76	0.377	
	Deflection (in.) per pound $\Delta_p = 2(\text{Sum})$								Sum = 0.451
	Stiffness of Sub-truss 2 = $(1/\Delta_p) = 1.109 \times 10^6$ lbs/in.								
B = Stiffness of Sub-truss 2 / (Stiffness of Sub-truss 1 + Stiffness of Sub-truss 2) = 0.49									

Notes: Positive sign (+) represents tension; Negative sign (-) represents compression.

E_{ct} for tension tie members

E_{cc} for compression strut members

Table 4.3, Distribution Factor B for the CASTM with Diagonal Steel Bars
(Geometry of Test Specimens)

$\frac{A_{SF}}{A_{SH}}$	$\frac{A_{SD}}{A_{SH}}$	B	
		By Virtual Work Analysis	By Eq. (16)
0.5	0.33	0.22	0.21
0.5	0.67	0.36	0.35
0.5	1.00	0.45	0.44
0.5	1.33	0.5	0.52
0.5	1.67	0.54	0.57
0.67	0.33	0.2	0.2
0.67	0.67	0.33	0.33
0.67	1.00	0.42	0.43
0.67	1.33	0.49	0.5
0.67	1.67	0.53	0.56
0.75	0.33	0.19	0.19
0.75	0.67	0.32	0.33
0.75	1.00	0.41	0.42
0.75	1.33	0.46	0.49
0.75	1.67	0.50	0.55
1	0.33	0.17	0.18
1	0.67	0.30	0.31
1	1.00	0.39	0.4
1	1.33	0.45	0.47
1	1.67	0.49	0.53
1.33	0.33	0.16	0.17
1.33	0.67	0.28	0.29
1.33	1.00	0.37	0.38
1.33	1.33	0.44	0.44
1.33	1.67	0.47	0.5
1.5	0.33	0.16	0.16
1.5	0.67	0.28	0.28
1.5	1.00	0.36	0.36
1.5	1.33	0.43	0.43
1.5	1.67	0.49	0.49

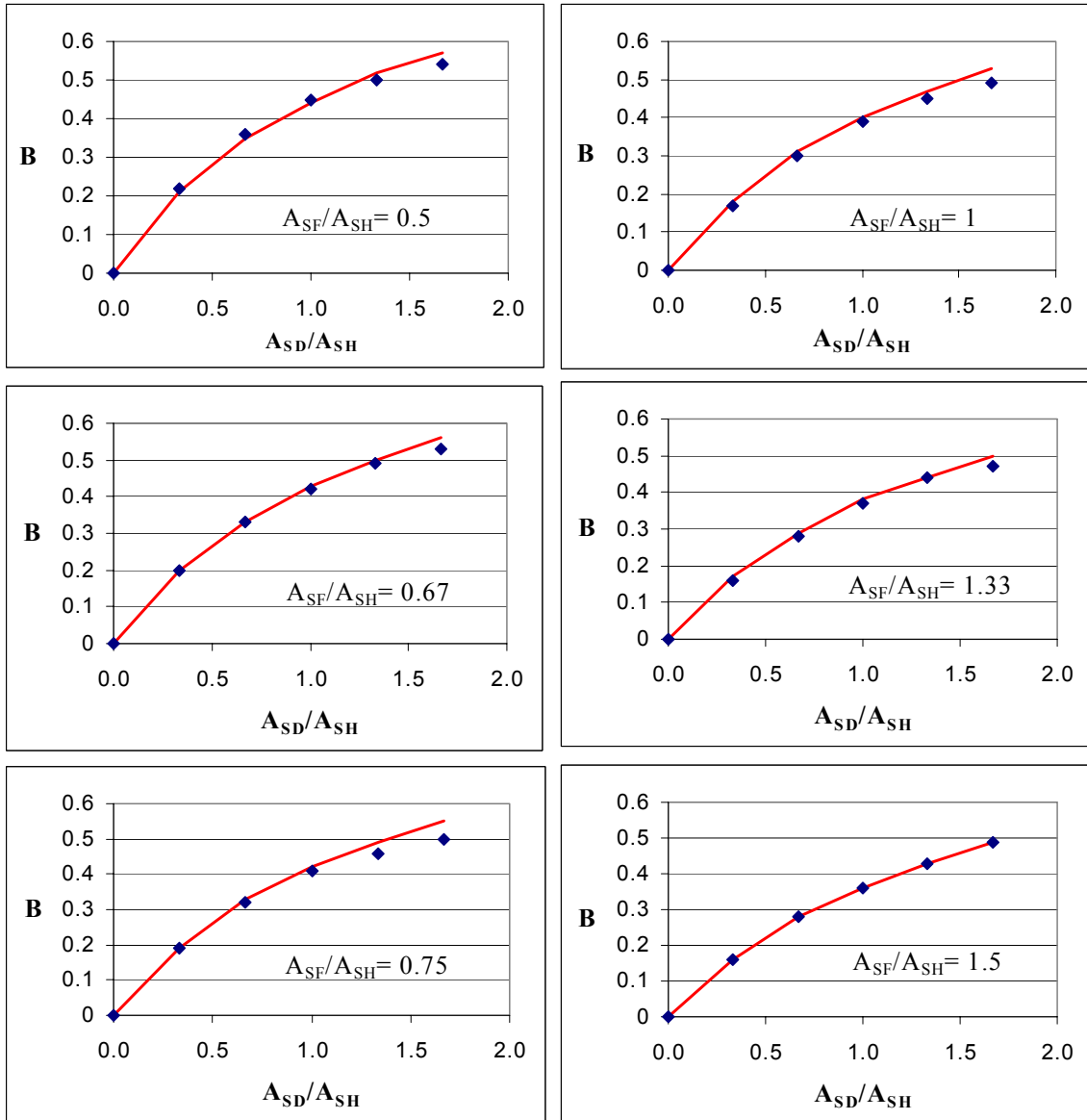


Fig. 4.8 Comparison of Distribution Factor B Calculated by Eq. (4-16)

with Rigorous Structural Analysis

The distribution factor B was also investigated by varying the geometry of the two sub-trusses in the CASTM. A new CASTM with an added mid-lengths of 17.25 in. (between the two loads P) is sketched in Fig. 4.9. The comparisons between the predictions of Eq. (4-16) and the

rigorous structural analysis are shown in Table 4.4 and Fig. 4.10. Again, the predictions of Eq. (4-16) agree very well with the rigorous structural analysis.

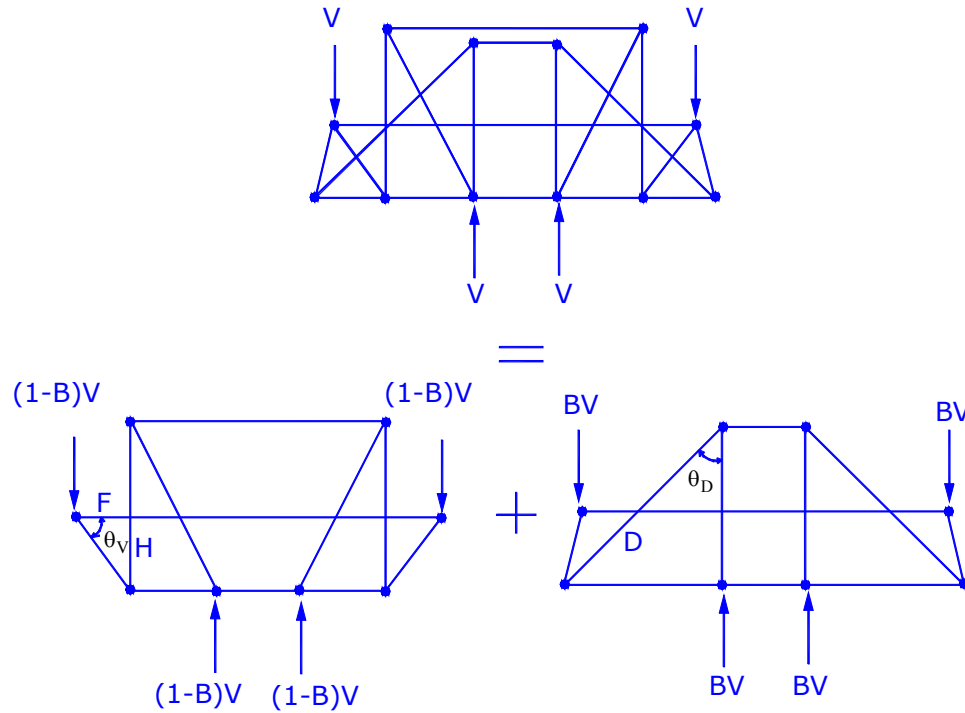


Fig. 4.9 CASTM with Diagonal Bars Simulating Specimens with Longer Mid-Length

Table 4.4, Distribution Factor B for the CASTM with Diagonal Steel Bars
(Geometry of Specimens with Added Mid-Lengths)

$\frac{A_{SF}}{A_{SH}}$	$\frac{A_{SD}}{A_{SH}}$	B	
		By Virtual Work Analysis	By Eq. (16)
0.5	0.33	0.24	0.21
0.5	0.67	0.39	0.35
0.5	1.00	0.49	0.44
0.5	1.33	0.56	0.52
0.5	1.67	0.62	0.57
0.67	0.33	0.22	0.2
0.67	0.67	0.36	0.33
0.67	1.00	0.46	0.43
0.67	1.33	0.53	0.5
0.67	1.67	0.58	0.56
0.75	0.33	0.21	0.19
0.75	0.67	0.35	0.33
0.75	1.00	0.44	0.42
0.75	1.33	0.51	0.49
0.75	1.67	0.57	0.55
1	0.33	0.19	0.18
1	0.67	0.32	0.31
1	1.00	0.41	0.4
1	1.33	0.49	0.47
1	1.67	0.54	0.53
1.33	0.33	0.18	0.17
1.33	0.67	0.3	0.29
1.33	1.00	0.39	0.38
1.33	1.33	0.46	0.44
1.33	1.67	0.52	0.5
1.5	0.33	0.17	0.16
1.5	0.67	0.29	0.28
1.5	1.00	0.38	0.36
1.5	1.33	0.45	0.43
1.5	1.67	0.51	0.49

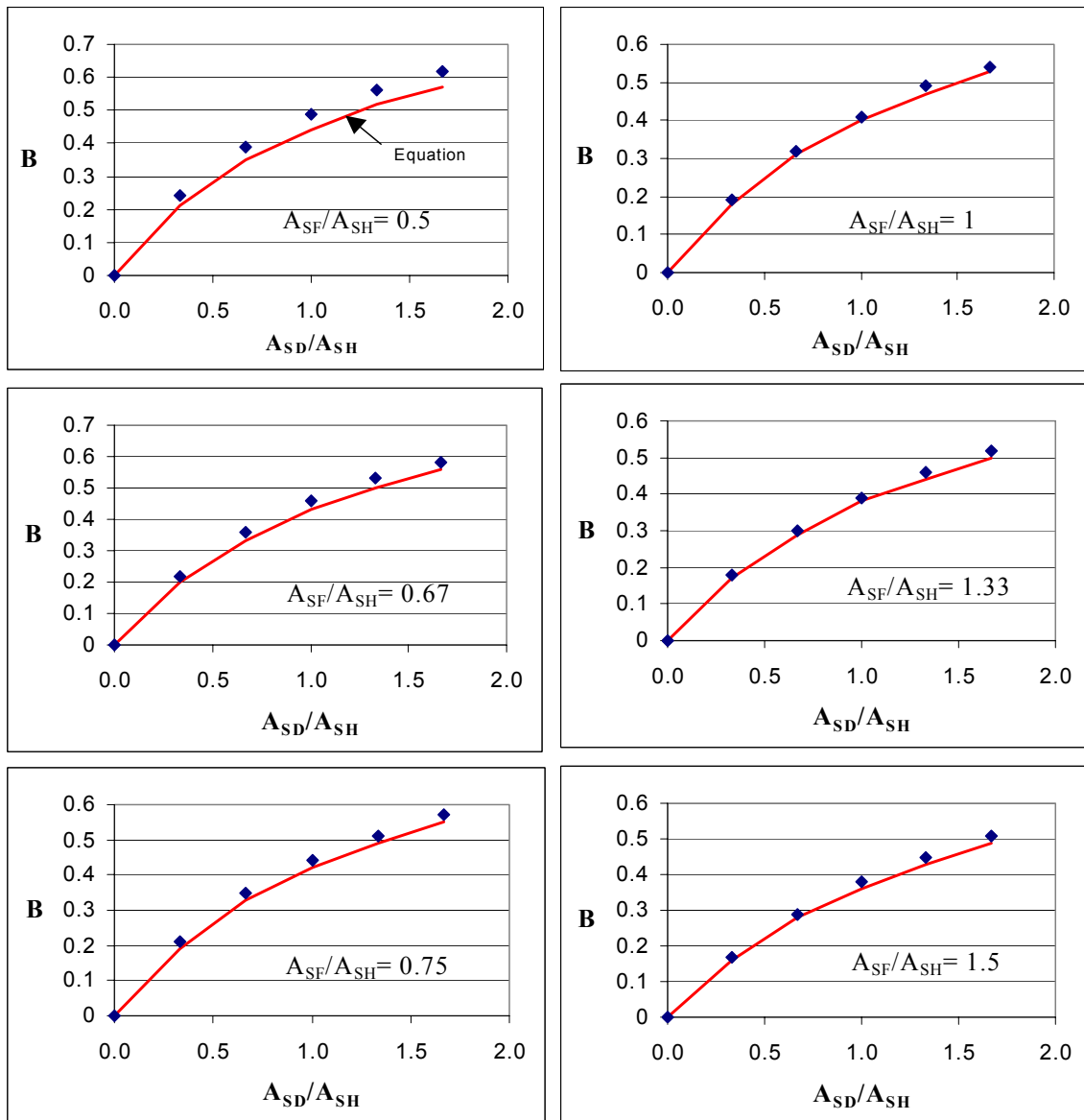


Fig. 4.10 Comparison of Distribution Factor B Calculated by Eq. (4-16)

with Rigorous Structural Analysis

4.3.4 Design Criteria of the CASTM with Diagonal Bars

The diagonal crack width w can be predicted by CASTM as follows:

$$w = L_{HF} \varepsilon_{HF} \quad (4-18)$$

where

w = predicted diagonal crack width (in.)

L_{HF} = CASTM gauge length for calculated hanger and flexural steel strains
 $= 9500 \varepsilon_{HF} - 3.0$ (in.)

ε_{HF} = diagonal crack strain calculated by hanger and flexural strains $= \sqrt{\varepsilon_H^2 + \varepsilon_F^2}$

ε_H = hanger strain or strain in the vertical direction $= \frac{(1 - B)V}{E_S A_{SH} + E_C A_{CH}}$

ε_F = flexural strain or strain in the horizontal direction $= \frac{(1 - B)V \cot \theta_V}{E_S A_{SF} + E_C A_{CF}}$

V = applied service load at each ledge (in pounds)

θ_V = Angle between flexural steel bars and the diagonal strut at the point of load V

B = distribution factor for diagonal bars $= \frac{A_{SD}}{A_{SH} + 0.5A_{SF} + A_{SD}}$

A_{SD} = total cross-sectional area of diagonal reinforcement at each ledge (in.²)

A_{SH} = total cross-sectional area of hanger reinforcement at each ledge (in.²)

A_{SF} = total cross-sectional area of flexural reinforcement at each ledge (in.²)

A_{CH} = total effective concrete area surrounding hanger reinforcement (in.²)

A_{CF} = total effective concrete area surrounding flexural reinforcement (in.²)

$$E_S = 29,000,000 \text{ psi}$$

$$E_C = 57,000\sqrt{f'_C} \text{ (psi) for compression and } 1,866\sqrt{f'_C} \text{ (psi) for tension}$$

$$f'_C = \text{concrete cylinder compressive strength (psi)}$$

The design criteria of CASTM *with* diagonal bars (section 4.3.4) are identical to those *without* diagonal bars (Section 4.2.5), except that the former involves the distribution factor B. When B is taken as zero, the CASTM *with* diagonal bars reduces to the CASTM *without* diagonal bars.

4.4 Comparison of the CASTM with Test Results

Eq. (4-18) can be used to calculate the diagonal crack strains at service load stage. The predicted results are shown in Fig. 4.11. It can be seen that the CASTM predictions match the test results very well. Table 4.5 lists the predictions by CASTM and the test results at the mid-point of the service load range. This comparison is also shown graphically in Fig. 4.12. It can be concluded that the predictions are well substantiated by the test results.

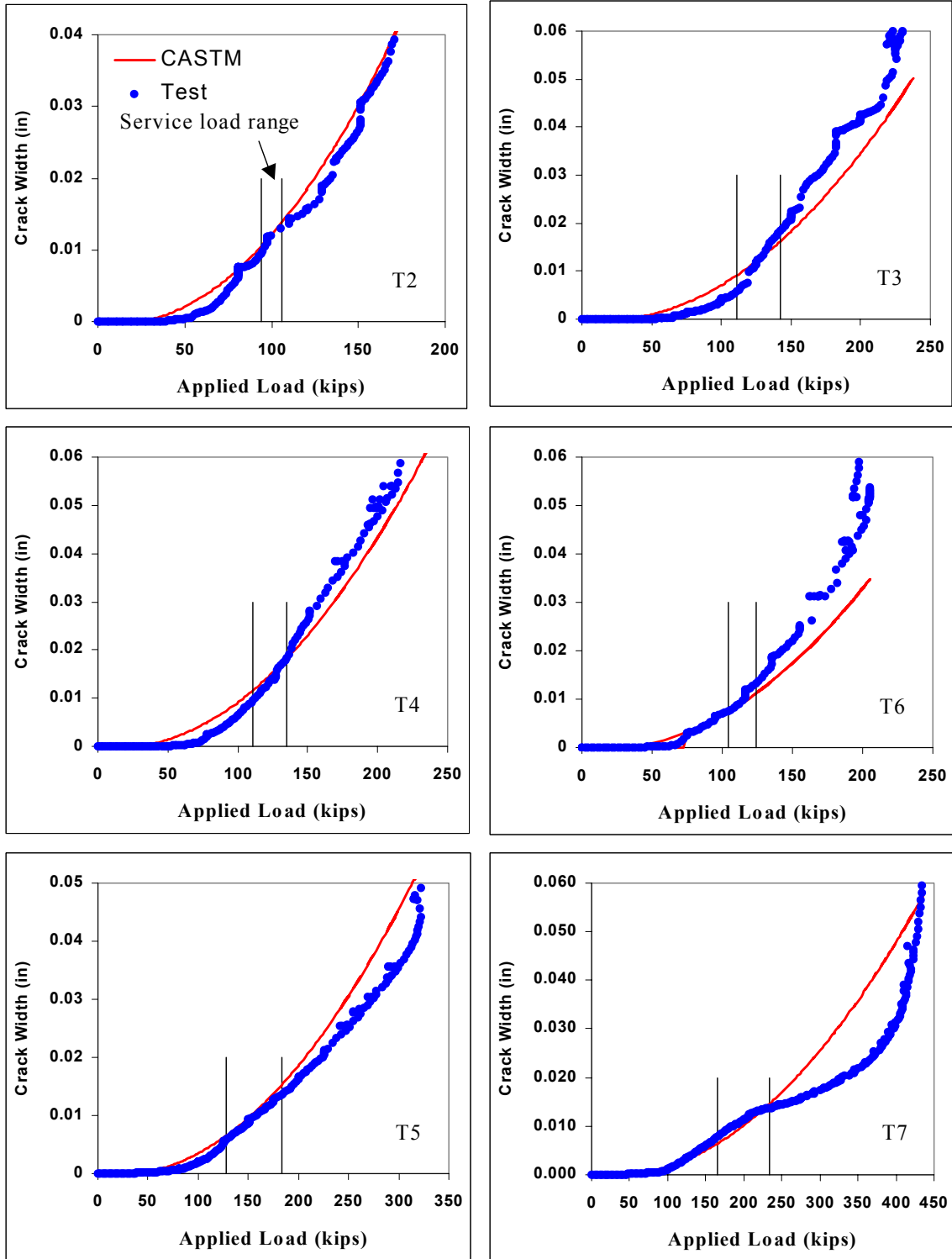


Fig. 4.11 Comparison of CASTM with Tests

Table 4.5 Cracking Width by Prediction and Test at the Mid-point of Service Load Range

Specimen	Steel bar				Service Load (kips)	Test (in.)		Prediction (in.)
	H	F	D	S		E or W Ends	Average	
T2-E	3	3	0	2	100	0.0107	0.0120	0.0120
T2-W	3	3	0	2	100	0.0132		
T3-E	5	3	0	2	127	0.0107	0.0127	0.0126
T3-W	5	3	0	2	127	0.0146		
T4-E	3	5	0	0	123	0.0099	0.0135	0.0148
T4-W	3	5	0	0	123	0.0170		
T5-E	3	3	3	0	156	0.0100	0.0099	0.0105
T5-W	3	3	3	0	156	0.0097		
T6-E	5	3	0	0	114	0.0093	0.0096	0.0093
T6-W	5	3	0	0	114	0.0099		
T7-E	3	3	5	0	200	0.0103	0.0113	0.0102
T7-W	3	3	5	0	200	0.0123		

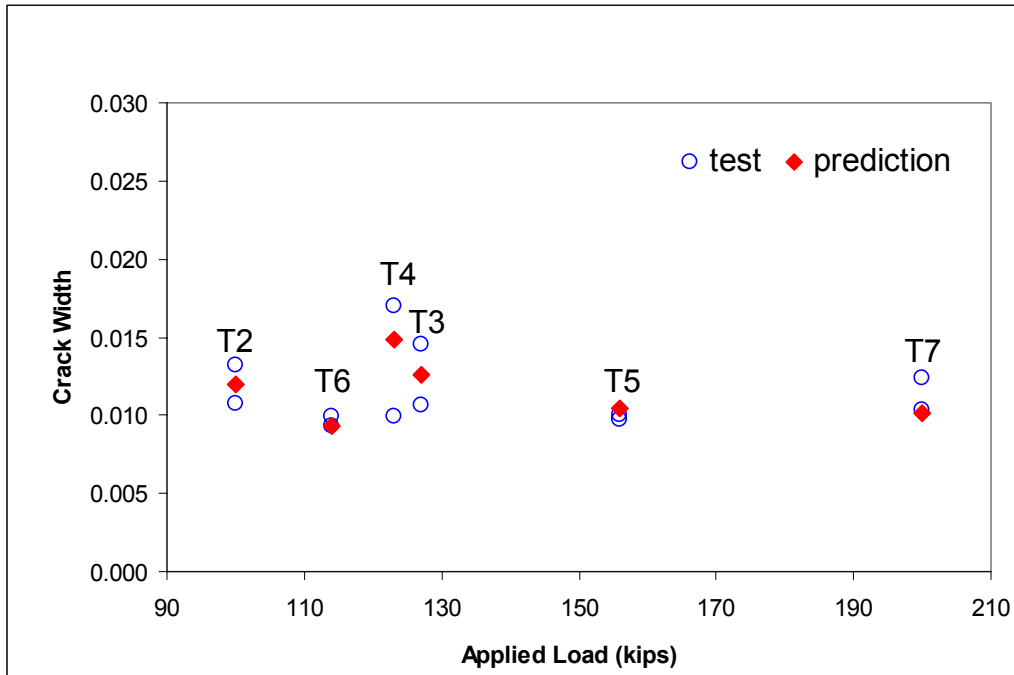


Fig. 4.12 Comparison of Crack Width by CASTM and the Test

REFERENCES

1. AASHTO, (1996). Standard Specifications for Highway Bridges, 16th Ed., American Association of State Highway Transportation Officials Washington D.C.
2. ACI-318, (1995). Building Code Requirements for Reinforced Concrete (ACI 3318-95) and Commentary (ACI 318R-95), American Concrete Institute, Farmington Hill, MI.
3. Mirza, A. S. and Furlong, R. W. (1985). “Design of Reinforced and Prestressed Concrete Inverted T Beams for Bridge Structures”, PCI Journal, Vol. 30. No. 4, July-August, pp. 112-136.
4. Schlaich, J., Schafer, K. and Jennewein, M., (1985). “Toward a Consistent Design of Structural Concrete ”, PCI Journal, May-June, pp. 77-150.